

## Physical mechanisms for vertical-CLVD earthquakes at active volcanoes

Ashley Shuler,<sup>1,2,3</sup> Göran Ekström,<sup>1,2</sup> and Meredith Nettles<sup>1,2</sup>

Received 24 August 2012; revised 8 February 2013; accepted 13 February 2013; published 26 April 2013.

[1] Many volcanic earthquakes large enough to be detected globally have anomalous focal mechanisms and frequency content. In a previous study, we examined the relationship between active volcanism and the occurrence of a specific type of shallow, non-double-couple earthquake. We identified 101 earthquakes with vertical compensated-linear-vector-dipole (vertical-CLVD) focal mechanisms that took place near active volcanoes between 1976 and 2009. The majority of these earthquakes, which have magnitudes  $4.3 \leq M_W \leq 5.8$ , are associated with documented episodes of volcanic unrest. Here we further characterize vertical-CLVD earthquakes and explore possible physical mechanisms. Through teleseismic body-wave analysis and examination of the frequency content of vertical-CLVD earthquakes, we demonstrate that these events have longer source durations than tectonic earthquakes of similar magnitude. We examine the covariance matrix for one of the best-recorded earthquakes and confirm that the isotropic and pure vertical-CLVD components of the moment tensor cannot be independently resolved using our long-period seismic data set. Allowing for this trade-off, we evaluate several physical mechanisms that may produce earthquakes with deviatoric vertical-CLVD moment tensors. We find that physical mechanisms related to fluid flow and volumetric changes are incompatible with seismological, geological, and geodetic observations of vertical-CLVD earthquakes. However, ring-faulting mechanisms explain many characteristics of vertical-CLVD earthquakes, including their seismic radiation patterns, source durations, association with volcanoes in specific geodynamic environments, and the timing of the earthquakes relative to volcanic activity.

**Citation:** Shuler, A., G. Ekström, and M. Nettles (2013), Physical mechanisms for vertical-CLVD earthquakes at active volcanoes, *J. Geophys. Res. Solid Earth*, 118, 1569–1586, doi:10.1002/jgrb.50131.

### 1. Introduction

[2] As magmas ascend from depth to intrude the crust or erupt on the surface, many different types of volcanic earthquakes are produced by processes such as brittle fracture, fluid flow, mass transport, and volumetric changes [e.g., *Chouet et al.*, 2003; *McNutt*, 2005; *Kumagai*, 2009; *Zobin*, 2011]. By observing, analyzing and interpreting these earthquakes, we can learn about the stress and strain conditions inside the edifices and magmatic plumbing systems of active volcanoes, an essential step for forecasting volcanic eruptions and assessing volcanic hazards. Although most volcanic earthquakes are small and only recorded by local monitoring

networks, occasionally volcanoes generate earthquakes large enough to be recorded on regional and global seismic networks [*McNutt*, 2000; *Zobin*, 2011]. Many of the largest volcanic earthquakes have been shown to have anomalous source properties, such as unusual seismic radiation patterns or frequency content [*Filson et al.*, 1973; *Francis*, 1974; *Dreger et al.*, 2000; *Kumagai et al.*, 2001; *Minson et al.*, 2007].

[3] In this paper and in our companion paper [*Shuler et al.*, 2013], hereafter referred to as Paper 1, we investigate some of the largest and most unusual volcanic earthquakes, those with vertical compensated-linear-vector-dipole (vertical-CLVD) focal mechanisms. By definition, vertical-CLVD earthquakes have deviatoric moment tensors with large non-double-couple components dominated by vertical compression or extension. Vertical-CLVD earthquakes are rarely observed, but commonly associated with volcanoes and volcanic unrest. Prior to our study in Paper 1,  $M_W \geq 5$  vertical-CLVD earthquakes had been identified near six volcanic centers around the world [*Kanamori et al.*, 1993; *Ekström*, 1994; *Nettles and Ekström*, 1998; *Shuler and Ekström*, 2009]. At Smith Rock, a submarine volcano in the Izu-Bonin arc, a vertical-CLVD earthquake produced a disproportionately large tsunami [*Kanamori et al.*, 1993], and at Bárðarbunga volcano in Iceland [*Nettles and Ekström*, 1998]

<sup>1</sup>Lamont-Doherty Earth Observatory of Columbia University, New York, New York, USA.

<sup>2</sup>Department of Earth and Environmental Sciences, Columbia University, New York, New York, USA.

<sup>3</sup>Department of Earth and Planetary Sciences, University of California Santa Cruz, Santa Cruz, California, USA.

Corresponding author: A. Shuler, Department of Earth and Planetary Sciences, University of California Santa Cruz, 1156 High Street, Santa Cruz, CA 95064, USA. (ashuler@ucsc.edu)

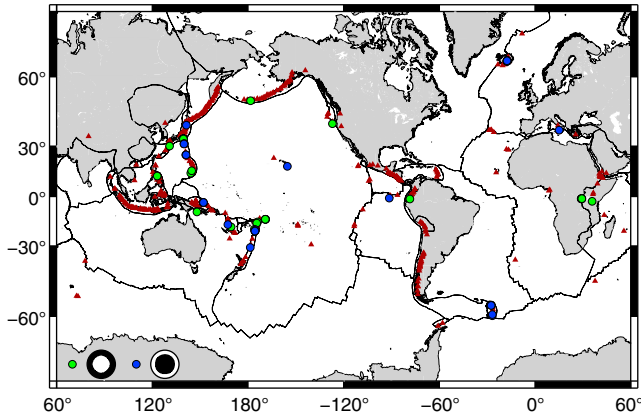


**Figure 1.** Map showing the locations of 101 vertical-CLVD earthquakes identified in Paper 1, including those from *Nettles and Ekström* [1998] and *Shuler and Ekström* [2009]. Vertical-P earthquakes are plotted as green circles and vertical-T earthquakes as blue circles. Maroon triangles indicate the locations of 429 volcanoes with eruptions later than 1900 documented by the Global Volcanism Project [Siebert and Simkin, 2002]. Plate boundaries are from *Bird* [2003].

and Nyiragongo volcano in the East African Rift [Shuler and Ekström, 2009], vertical-CLVD earthquakes are associated with damaging fissure eruptions.

[4] In some cases, apparent non-double-couple focal mechanisms may result from unmodeled seismic velocity heterogeneity in the earthquake source region. However, such velocity heterogeneity is unlikely to be the cause of moderate-to-large vertical-CLVD earthquakes. In Paper 1 and the work of *Nettles and Ekström* [1998] and *Shuler and Ekström* [2009], focal mechanisms were determined using long-period (40–150 s) body- and surface-wave data, which are largely insensitive to the small-scale structures associated with magmatic plumbing systems. Detailed studies of the Tori Shima, Bárdarbunga, and Nyiragongo earthquakes have confirmed that the vertical-CLVD focal mechanisms retrieved for those regions are representative of an anomalous earthquake source.

[5] In order to assess the relationship between vertical-CLVD earthquakes and volcanic unrest systematically, we searched in Paper 1 for additional examples of shallow vertical-CLVD earthquakes located near volcanoes with documented eruptions in the last ~100 years. We investigated nearly 400 target earthquakes from the Global Centroid Moment Tensor catalog (GCMT, 1976–2009) and the Surface Wave catalog (1991–2009) of *Ekström* [2006], and used well-defined criteria to classify earthquakes as vertical-CLVD. We required vertical-CLVD earthquakes to have dominant pressure or tension axes that plunge more steeply than  $60^\circ$  and deviatoric moment tensors that are distinctly non-double couple with  $|\epsilon| > 0.20$ , where

$$\epsilon = -\lambda_2 / \max(|\lambda_1|, |\lambda_3|), \quad (1)$$

and  $\lambda_1$ ,  $\lambda_2$ , and  $\lambda_3$  are the diagonal elements of the moment tensor in the principal axes coordinate system, ordered such that  $\lambda_1 \geq \lambda_2 \geq \lambda_3$ . Vertical-P earthquakes have dominant pressure axes, and vertical-T earthquakes have dominant tension axes.

[6] All together, we identified 101 vertical-CLVD earthquakes located near active volcanoes (Figure 1), approximately two thirds of which are vertical-P type and one third are vertical-T type. These earthquakes have magnitudes  $4.3 \leq M_w \leq 5.8$  and shallow focal depths. We found that most vertical-CLVD earthquakes take place in subduction zones, although a small number are located in continental rifts, along mid-ocean ridges, and in regions of hot spot volcanism. Vertical-CLVD earthquakes are predominantly associated with volcanoes that erupt magmas with low silica content, and the most common source volcanoes are strato-volcanoes and submarine volcanoes with caldera structures.

[7] We also found that the vast majority of vertical-CLVD earthquakes are linked spatially and temporally to documented episodes of volcanic unrest at nearby volcanoes, which suggests that these events are generated by magmatic and/or volcano-tectonic processes. Vertical-CLVD earthquakes are associated with volcanogenic tsunamis, volcanic earthquake swarms, effusive and explosive eruptions, and caldera collapse. In general, vertical-P earthquakes follow episodes of volcanic unrest, whereas vertical-T earthquakes occur before eruptive activity initiates at a source volcano. This may indicate that one type of vertical-CLVD earthquake occurs in response to volcanic eruptions or large-scale magma intrusions, whereas the other occurs in association with magma ascent.

[8] To date, two main classes of physical mechanisms have been presented to explain vertical-CLVD earthquakes. The first class is composed of mechanisms related to fluid flow and volumetric changes. Examples of mechanisms in this class include rapid magma injection [Kanamori et al., 1993; Konstantinou et al., 2003] or withdrawal, rapid expansion or contraction, and volume or mass exchange between two magma chambers [Tkalčić et al., 2009]. In cases where there is no net volume change, deviatoric moment tensors are appropriate. However, earthquakes produced by uncompensated volume changes are expected to have moment tensors with a non-zero isotropic component.

[9] The second class is composed of ring-faulting mechanisms, in which vertical-CLVD earthquakes are produced by shear failure on curved or cone-shaped fault structures [Ekström, 1994; Nettles and Ekström, 1998; Shuler and Ekström, 2009]. Although dip-slip motion along ring faults can be triggered by the inflation or deflation of shallow magma chambers, no net volume change is expected for earthquakes produced by pure ring-faulting mechanisms, so these events should be modeled well using deviatoric moment tensors.

[10] Following standard GCMT procedure, in Paper 1 we constrained the isotropic component to equal zero when calculating centroid-moment-tensor (CMT) solutions and identified vertical-CLVD earthquakes according to the properties of their deviatoric moment tensors. However, because there is a known trade-off between the isotropic and pure vertical-CLVD components of the moment tensor for shallow earthquakes [Kawakatsu, 1996], some earthquakes that we identify as vertical-CLVD could have underlying source processes dominated by isotropic components rather than vertical-CLVD components. At Miyakejima and Tungurahua volcanoes, full moment-tensor solutions for vertical-CLVD earthquakes calculated using local seismic data are dominated by isotropic components, and models spanning

both classes of physical mechanisms have been proposed for individual events [Kikuchi *et al.*, 2001; Kumagai *et al.*, 2001, 2010]. Clearly, a discussion of the physical mechanisms of vertical-CLVD earthquakes requires consideration of the isotropic component of the moment tensor.

[11] Because the isotropic and pure vertical-CLVD components of the moment tensor cannot be independently resolved using long-period seismic data, additional information is needed to evaluate possible source mechanisms for vertical-CLVD earthquakes. The spatial and temporal relationships between vertical-CLVD earthquakes and volcanism that we identified in Paper 1 provide some constraints. Additional important information would be provided by better knowledge of the source durations of these events. From previous studies, there are several indications that vertical-CLVD earthquakes may have unusually long source processes. In order to model the teleseismic body waves of vertical-CLVD earthquakes at Smith Rock [Kanamori *et al.*, 1993] and Bárðarbunga [Nettles and Ekström, 1998] volcanoes, source durations exceeding the average magnitude-duration relationship for tectonic earthquakes [Ekström *et al.*, 1992] are required. Additionally, the frequency spectra of vertical-CLVD earthquakes at Nyiragongo volcano indicate that these events are depleted in high-frequency energy and have lower corner frequencies than tectonic earthquakes with similar magnitudes and locations [Shuler and Ekström, 2009]. Similarly, waveforms from local and regional seismic stations indicate that the vertical-CLVD earthquakes associated with the incremental caldera collapse of Miyakejima volcano have smooth source-time functions lasting ~30–65 s [Kikuchi *et al.*, 2001; Kumagai *et al.*, 2001; Ohminato and Kumagai, 2001].

[12] In this paper, we explore a range of physical processes that may produce volcanic earthquakes with deviatoric vertical-CLVD moment tensors. We perform additional detailed analysis on the data set of 86 vertical-CLVD earthquakes studied in Paper 1 and combine these results with those for the 15 earthquakes studied by Nettles and Ekström [1998] and Shuler and Ekström [2009]. We begin by systematically examining the broadband body waves of vertical-CLVD earthquakes to gain additional constraints on their source durations and frequency content. We calculate full moment-tensor solutions for vertical-CLVD earthquakes and investigate the trade-off between the isotropic and pure vertical-CLVD components of the moment tensor for our data set. We then examine several physical mechanisms that have been suggested to explain the anomalous seismic radiation patterns of vertical-CLVD earthquakes, including slip on ring faults, volume exchange between two reservoirs, opening and closing of tensile cracks, and other types of volumetric sources. Finally, we evaluate these mechanisms in light of our observations of vertical-CLVD earthquakes and their relationships to volcanoes and volcanic unrest.

## 2. Data and Analysis

[13] In Paper 1, we used standard GCMT methodology [Dziewonski *et al.*, 1981; Ekström *et al.*, 2012] and seismic data from regional and global networks to identify 86 shallow vertical-CLVD earthquakes located near active volcanoes. Because we used long-period seismic data and the

vertical-CLVD earthquakes are shallow, several source parameters were not resolved in detail. The centroid depths of the vertical-CLVD earthquakes were fixed to 12 km during the CMT inversion, and the earthquake durations were estimated using an empirical moment-duration relationship [Ekström *et al.*, 2012]. Likewise, we constrained the isotropic component of the moment tensor to equal zero and calculated deviatoric moment-tensor solutions. At long periods and teleseismic distances, the isotropic and pure vertical-CLVD components of the moment tensor generate very similar seismic radiation, so these components cannot be independently resolved [Mendiguren and Aki, 1978; Kanamori and Given, 1981; Kawakatsu, 1996; Dufumier and Rivera, 1997]. The isotropic component is expected to be small for tectonic earthquakes, but in volcanic and geothermal areas, earthquakes with statistically significant isotropic components have been observed [e.g., Miller *et al.*, 1998a; Dreger *et al.*, 2000; Foulger *et al.*, 2004; Minson and Dreger, 2008].

[14] In section 2.1, we model the teleseismic body waves of vertical-CLVD earthquakes in order to obtain estimates of their source durations; in doing so, we also obtain better constraints on their depths. We gain additional insight into the source processes of vertical-CLVD earthquakes by examining differences in the frequency content and magnitude distribution of earthquakes reported in the GCMT and Surface Wave catalogs. In section 2.2, we calculate full moment-tensor solutions for the vertical-CLVD earthquakes reported in Paper 1 and evaluate the trade-off between the isotropic and pure vertical-CLVD components of the moment tensor for our data set.

### 2.1. Earthquake Source Duration and Magnitude Distribution

[15] In order to obtain better constraints on the source durations and focal depths of vertical-CLVD earthquakes, we attempt to model the teleseismic body waves for the 63 earthquakes from Paper 1 that have  $M_W \geq 5.1$ . We use seismic records from the Data Management Center of the Incorporated Research Institutions for Seismology (IRIS) and the method of Ekström [1989] to invert broadband  $P$  and  $SH$  waveforms for focal mechanism, moment-rate function and focal depth. We include the point-source moment tensors from Paper 1 as soft constraints to ensure that focal mechanisms calculated from the broadband data are compatible with our preferred solutions calculated by the CMT inversions using long-period data. We assign each solution a quality based on the fit to the data and the number of waveforms used in the broadband body-wave modeling. Solutions with A quality have the best fit to the data, especially for the initial  $P$  waves and the first crustal reflections. Solutions with B and C qualities have poorer fits and therefore greater uncertainties associated with estimates of depth and source duration. An example of an A-quality solution is shown in Figure 2.

[16] For most of the vertical-CLVD earthquakes we study, we find that the broadband body waves are of lower amplitude than the background noise. However, we are able to model the body waves for 18 earthquakes, 3 vertical-P events and 15 vertical-T events (Table 1). In general, we find the body waves to be emergent and dominated by low-frequency energy. We do not observe the impulsive direct

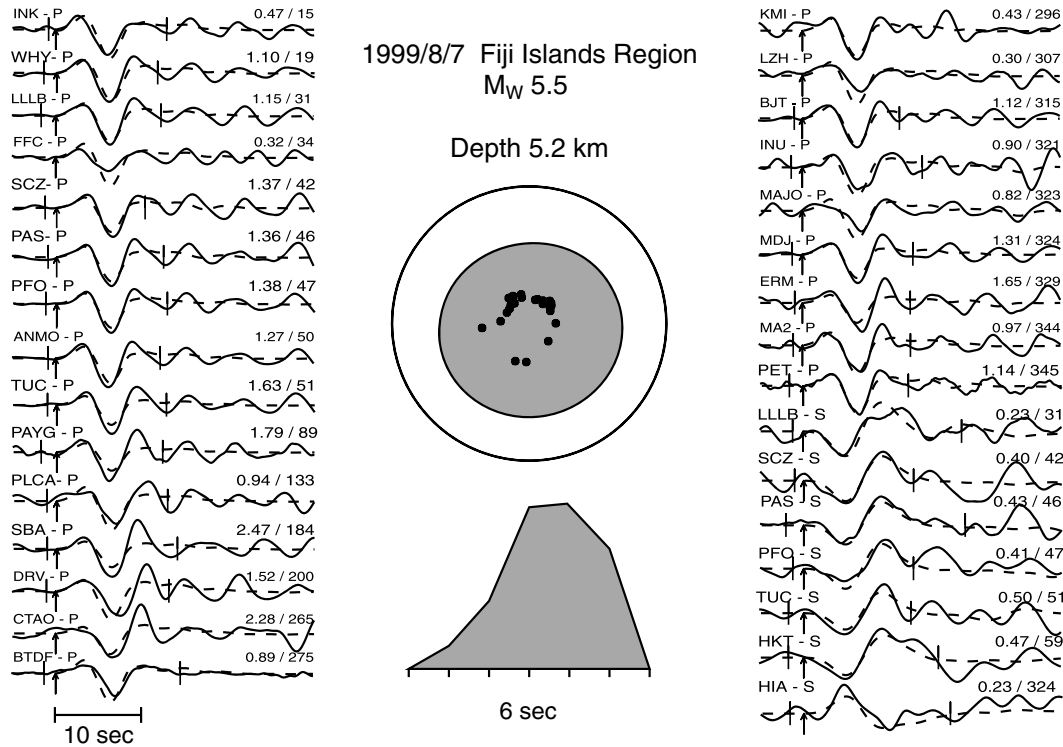


**Figure 2.** Source-duration and focal-depth analysis for the  $M_W$  5.5 vertical-T earthquake that occurred on 7 August 1999 near an Unnamed volcano 0403-01 (in IAVCEI’s Catalog of Active Volcanoes of the World) in the Fiji Islands region. Solid lines show broadband teleseismic  $P$  and  $SH$  waveforms modeled for this event; dashed lines are synthetic seismograms. Brackets across the waveform show the portions of the seismograms used in the inversion, and arrows indicate the picked first arrivals. The station name, data type, maximum amplitude (in microns), and azimuth from source (in degrees) are printed above each waveform. Waveforms are ordered by data type and azimuth. The focal mechanism and moment-rate function determined in the body-wave inversion are plotted in the center of the figure. Black dots on the focal mechanism show where the modeled waveforms exited the focal sphere. The estimated focal depth of the earthquake is  $\sim 5.2$  km below sea level or  $\sim 4.7$  km into the crust. This is an example of an A-quality broadband body-wave solution.

arrivals and surface reflections typical for earthquakes in this magnitude range. For our preferred solutions, source durations range from 4 to 10 s and focal depths range from 4 to 8 km, varying by 1–2 km for multiple vertical-CLVD earthquakes in the same location. Our estimates of focal depth and source duration are consistent with those of *Nettles and Ekström* [1998], who reported focal depths of 3–7 km and source durations of 4–7 s for ten  $5.1 \leq M_W \leq 5.6$  vertical-T earthquakes near Bárðarbunga volcano. We find that all of the vertical-CLVD earthquakes have moment-rate functions with smoothly varying, approximately triangular shapes, except for the  $M_W$  5.6 vertical-P earthquake that occurred in East Papua New Guinea on 29 June 1999. This earthquake has the longest source duration of our data set, 10 s, and appears to be composed of several subevents.

[17] Due to the partial overlap of direct and reflected phases, there is a trade-off between focal depth and source duration. Our preferred solutions are listed in Table 1, but for most earthquakes, the broadband data can be fit nearly as well using shallower focal depths and slightly longer source time functions. We estimate that the uncertainties associated with focal-depth and source-duration estimates are approximately 2 km and 1 s, respectively.

[18] For moderate-to-large shallow earthquakes, the global average relationship between source duration and scalar moment as derived from broadband body-wave modeling is

$$\tau = 4.52 \times 10^{-6} (M_0)^{1/3}, \quad (2)$$

where  $\tau$  is the source duration in s and  $M_0$  is the scalar moment in Nm [Ekström *et al.*, 2012]. As demonstrated in Figure 3, all of the vertical-CLVD earthquakes we are able to model have longer-than-average source durations, and therefore slower-than-average source processes, for their moment magnitudes. For example,  $M_W$  5.8 earthquakes have average source durations of  $\sim 4$  s, whereas we observe a source duration of  $\sim 8$  s for the  $M_W$  5.8 vertical-T earthquake that occurred near Curtis Island volcano in the Kermadec Islands on 17 February 2009. Although we are unable to model the broadband body waves for the remaining vertical-CLVD earthquakes, we can assess their source durations by examining the general frequency content of earthquakes reported in the GCMT and Surface Wave catalogs.

[19] Our lack of success in modeling more of the vertical-CLVD earthquakes is consistent with the pattern of longer-than-usual source durations. Twenty-six of the vertical-CLVD

**Table 1.** Results of Broadband Body-Wave Modeling<sup>a</sup>

| Earthquake Date and Time |    |    |    |    |      | Centroid Latitude | Centroid Longitude | Geographical Location         | $M_W$ | Depth (km) | Source Duration (s) | Solution Quality |
|--------------------------|----|----|----|----|------|-------------------|--------------------|-------------------------------|-------|------------|---------------------|------------------|
| Y                        | M  | D  | h  | m  | sec  |                   |                    |                               |       |            |                     |                  |
| 1978                     | 5  | 16 | 7  | 35 | 49.1 | 40.99             | 141.44             | Hokkaido, Japan               | 5.3   | 5.8        | 4                   | B                |
| 1984                     | 6  | 13 | 2  | 29 | 29.8 | 31.57             | 139.97             | South of Honshu, Japan        | 5.6   | 3.8        | 7                   | B                |
| 1990                     | 5  | 15 | 15 | 21 | 31.1 | -2.96             | 35.80              | Tanzania                      | 5.4   | 5.5        | 4                   | A                |
| 1992                     | 8  | 20 | 18 | 31 | 39.9 | 25.43             | 141.13             | Volcano Islands, Japan        | 5.2   | 7.3        | 6                   | B                |
| 1994                     | 1  | 16 | 10 | 18 | 41.5 | -20.62            | -175.20            | Tonga Islands                 | 5.3   | 4.1        | 4                   | A                |
| 1996                     | 9  | 4  | 18 | 16 | 7.7  | 31.51             | 139.99             | South of Honshu, Japan        | 5.7   | 5.2        | 8                   | A                |
| 1996                     | 9  | 9  | 4  | 34 | 21.9 | 30.44             | 130.95             | Kyushu, Japan                 | 5.7   | 7.7        | 8                   | A                |
| 1997                     | 9  | 5  | 3  | 23 | 17.0 | -56.41            | -27.47             | South Sandwich Islands Region | 5.4   | 5.2        | 7                   | C                |
| 1999                     | 6  | 29 | 5  | 50 | 9.2  | -9.59             | 147.97             | East Papua New Guinea         | 5.6   | 5.5        | 10                  | A                |
| 1999                     | 8  | 7  | 6  | 17 | 30.5 | -21.24            | -175.61            | Fiji Islands Region           | 5.5   | 5.2        | 6                   | A                |
| 2001                     | 1  | 18 | 20 | 17 | 17.4 | -56.31            | -27.43             | South Sandwich Islands Region | 5.3   | 4.9        | 6                   | C                |
| 2004                     | 11 | 10 | 10 | 35 | 38.0 | -21.26            | -175.62            | Fiji Islands Region           | 5.5   | 3.9        | 6                   | B                |
| 2005                     | 8  | 23 | 1  | 38 | 20.1 | -59.80            | -26.68             | South Sandwich Islands Region | 5.1   | 5.2        | 4                   | B                |
| 2005                     | 8  | 31 | 1  | 24 | 54.9 | -59.48            | -26.86             | South Sandwich Islands Region | 5.5   | 5.5        | 4                   | C                |
| 2006                     | 1  | 1  | 7  | 12 | 8.8  | 31.60             | 140.17             | Southeast of Honshu, Japan    | 5.6   | 5.2        | 7                   | A                |
| 2008                     | 6  | 12 | 13 | 10 | 14.7 | 25.53             | 141.18             | Volcano Islands, Japan        | 5.3   | 7.5        | 6                   | C                |
| 2009                     | 2  | 17 | 3  | 30 | 58.8 | -30.54            | -178.58            | Kermadec Islands, New Zealand | 5.8   | 6.4        | 8                   | B                |
| 2009                     | 5  | 26 | 0  | 49 | 42.9 | -21.24            | -175.62            | Fiji Islands Region           | 5.5   | 5.8        | 6                   | A                |

<sup>a</sup>Centroid times, locations, and magnitudes are from the CMT solutions presented in Paper 1. Depth and source-duration estimates are from broadband body-wave modeling. See text for explanation of solution quality.

earthquakes from Paper 1 are reported in the GCMT catalog. Initial hypocentral parameters for the vast majority of earthquakes in the GCMT catalog are provided by the United States Geological Survey (USGS) National Earthquake Information Center (NEIC), where event detection is based on the arrival times of high-frequency body waves. Since 2006, hypocentral parameters from the intermediate-period surface-wave event-detection algorithm of *Ekström* [2006] have been used for a small number of moderate-to-large earthquakes not detected by the USGS, but these events represent fewer than 3% of earthquakes reported annually in the GCMT catalog [Ekström et al., 2012]. All 18 earthquakes that we are able to model using broadband body-wave analysis are from the GCMT catalog with initial detections based on high-frequency body-wave phases from the NEIC.

[20] The remaining 60 vertical-CLVD earthquakes from Paper 1 are from two subsets of the Surface Wave catalog of *Ekström* [2006]. Category 1 earthquakes have surface-wave magnitudes,  $M_{SW}$  [Ekström, 2006], that are at least one magnitude unit larger than the body-wave magnitudes,  $m_b$ , reported in the International Seismological Center (ISC) Bulletin. Body-wave magnitudes are calculated at a period of  $\sim 1$  s, and surface-wave magnitudes are calculated between periods of 35 and 150 s. The discrepancy between these two magnitudes suggests that Category 1 vertical-CLVD earthquakes are depleted in high-frequency energy and have slow source processes.

[21] Category 2 earthquakes from the Surface Wave catalog are missing from the ISC and NEIC global seismicity catalogs but were detected and located using intermediate-period surface waves and the method of *Ekström* [2006]. Since the amplitudes of high-frequency body-wave phases of Category 2 earthquakes were too small to be detected by the ISC and NEIC, despite the fact that they have magnitudes up to  $M_W$  5.6, and since teleseismic surface waves are dominated by lower-frequency energy than body waves, these events likely have slow source processes. Observations of Category 2 vertical-CLVD earthquakes at Miyakejima, Stromboli, and Nyiragongo volcanoes support this interpretation. The largest

vertical-P earthquakes at Miyakejima have average source durations of  $\sim 50$  s [Kikuchi et al., 2001; Kumagai et al., 2001; Ohminato and Kumagai, 2001], which is  $\sim 20$  times longer than expected given their magnitudes of  $5.0 \leq M_W \leq 5.6$ . An  $M_W$  4.3 vertical-T earthquake at Stromboli has been described as a very-long-period event that lasted  $\sim 12$  s [D'Auria et al., 2006]. Likewise, vertical-P earthquakes at Nyiragongo are depleted in high-frequency energy and have lower corner frequencies than tectonic earthquakes with similar magnitudes and locations [Shuler and Ekström, 2009].

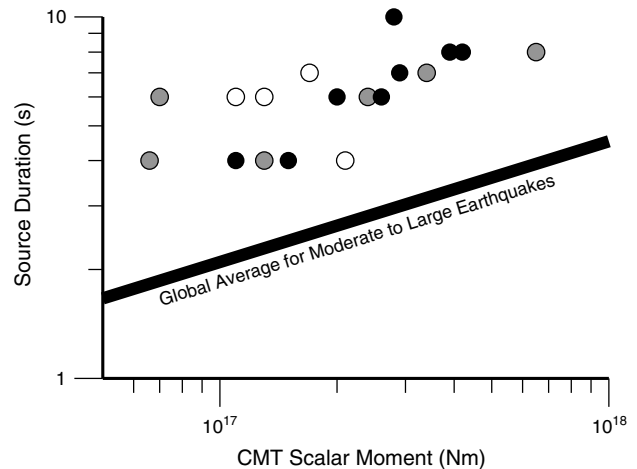


**Figure 3.** Log-log plot of the scalar moment (in Nm) and source duration (in s) of 18 vertical-CLVD earthquakes. The estimates of scalar moment are from the CMT solutions in Paper 1, and the estimates of source duration are from broadband body-wave modeling. The color of the circles indicates the quality of the broadband body-wave solutions. Black circles are for A-quality solutions, gray circles are for B-quality solutions, and white circles are for C-quality solutions. The thick black line shows the global average relationship between scalar moment and source duration for shallow, moderate-to-large earthquakes [Ekström et al., 2012].

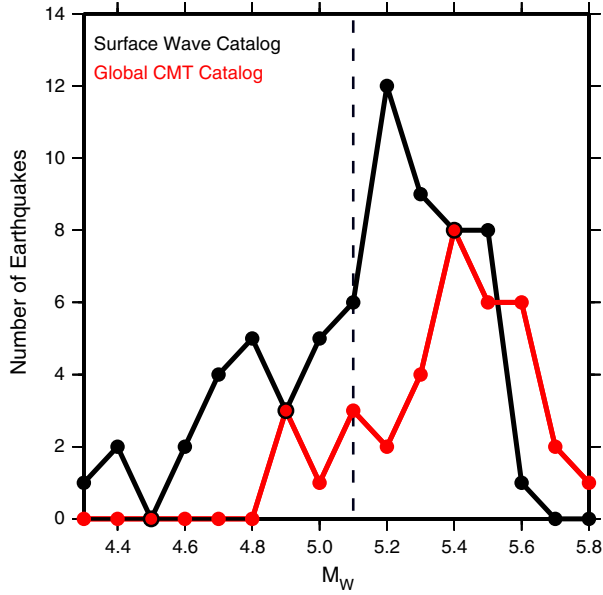


**Figure 4.** Distribution of vertical-CLVD earthquakes by source catalog and moment magnitude. Earthquakes are binned by 0.1 units of moment magnitude. Red dots and lines represent earthquakes from the Global CMT catalog, and black dots and lines represent earthquakes from the Surface Wave Catalog of *Ekström* [2006]. Included are vertical-CLVD earthquakes from *Nettles and Ekström* [1998], *Shuler and Ekström* [2009], and Paper 1, and the  $M_w$  values are taken from these studies. We draw a dashed black line at  $M_w$  5.1 because we are able to model the body waves for nearly all  $M_w \geq 5.1$  vertical-CLVD earthquakes from the Global CMT catalog, while we are not able to model any  $M_w \geq 5.1$  vertical-CLVD earthquakes from the Surface Wave catalog.

[22] Figure 4 shows the moment magnitude distributions for vertical-CLVD earthquakes by source catalog. Included are the 10 vertical-T earthquakes from Bárðarbunga volcano [*Nettles and Ekström*, 1998], which are reported in the GCMT catalog, and the 5 vertical-P earthquakes from Nyiragongo volcano [*Shuler and Ekström*, 2009], which are reported in the Surface Wave catalog. The GCMT catalog includes vertical-CLVD earthquakes with magnitudes as large as  $M_w$  5.8, and we are able to model the teleseismic body waves for nearly all earthquakes with magnitudes  $M_w \geq 5.1$ . Although the Surface Wave catalog includes vertical-CLVD earthquakes with magnitudes as large as  $M_w$  5.6, we are not able to model the teleseismic body waves for any of these earthquakes. This provides another indication that vertical-CLVD earthquakes in the Surface Wave catalog have long source durations, and suggests that they may have even slower source processes than vertical-CLVD earthquakes in the GCMT catalog. Since vertical-P earthquakes are predominantly from the Surface Wave catalog and vertical-T earthquakes are predominantly from the GCMT catalog, we infer that vertical-P earthquakes may have slower source processes than vertical-T earthquakes in general.

[23] The two magnitude distributions for vertical-CLVD earthquakes are similar to one another (Figure 4), but the distribution for the GCMT catalog is shifted  $\sim 0.2$  magnitude units higher than the distribution for the Surface Wave catalog. The low number of small-magnitude vertical-CLVD

earthquakes reported in each catalog is likely due to the magnitude of completeness, which varies as a function of time and geographical location. However, the small number of large-magnitude vertical-CLVD earthquakes is surprising. In 34 years of data from the GCMT catalog (1976–2009) and 19 years of data from the Surface Wave catalog (1991–2009), we have observed  $\sim 75$  earthquakes with magnitudes  $M_w \geq 5$  but no earthquakes with  $M_w \geq 6$ . This observation suggests that vertical-CLVD earthquakes do not follow the Gutenberg-Richter magnitude-frequency distribution [*Gutenberg and Richter*, 1944] with the global average  $b$ -value of 1.0 [*Frohlich and Davis*, 1993]. Since our catalog of vertical-CLVD earthquakes ends below  $M_w$  6, this may indicate that there is an upper limit on the source size for vertical-CLVD earthquakes at active volcanoes.

## 2.2. Trade-off Between Isotropic and Pure Vertical-CLVD Components

[24] For long-period teleseismic data, there is a trade-off between the isotropic and pure vertical-CLVD components of the moment tensor [*Mendiguren and Aki*, 1978; *Kanamori and Given*, 1981; *Kawakatsu*, 1996; *Dufumier and Rivera*, 1997]. We investigate this trade-off for our data set by calculating the unscaled covariance matrices following the method of *Kawakatsu* [1996].

[25] We begin with the inverse of the inner-product matrix,  $\mathbf{A}^{-1}$ , which can be calculated from synthetic waveforms using the centroid location of an earthquake and a distribution of available stations. The matrix  $\mathbf{A}^{-1}$  is related to the covariance matrix for the moment-tensor elements,  $\mathbf{C}_m$ , by a scalar:

$$\mathbf{C}_m = \sigma_d^2 \mathbf{A}^{-1}, \quad (3)$$

where  $\sigma_d^2$  is the variance of the data. In order to isolate the isotropic ( $I$ ) and pure vertical-CLVD components ( $C$ ), we rotate the diagonal elements of the moment tensor into a new basis where

$$I = \frac{1}{3} (M_{rr} + M_{\theta\theta} + M_{\phi\phi}) \quad (4)$$

$$C = \frac{1}{3} (M_{\theta\theta} + M_{\phi\phi} - 2M_{rr}) \quad (5)$$

$$D = \frac{1}{2} (M_{\theta\theta} - M_{\phi\phi}). \quad (6)$$

[26] As an example, we calculate  $\mathbf{A}^{-1}$  for one of the best-recorded vertical-CLVD earthquakes, an  $M_w$  5.6 vertical-P earthquake that took place at Miyakejima volcano on 2 August 2000. We use the centroid location for the earthquake and the same station locations, time windows, and frequency bands that were used to calculate the CMT solution in Paper 1. We include two data sets, body waves from 134 stations that were predominantly filtered from 40 to 150 s, and surface waves from 150 stations that were predominantly filtered from 50 to 150 s. Synthetic seismograms are calculated following standard GCMT procedure [*Dziewonski et al.*, 1981; *Arvidsson and Ekström*, 1998] and specifically the methods employed since 2004 [*Ekström et al.*, 2012].

[27] We calculate the eigenvalues and eigenvectors of  $\mathbf{A}^{-1}$ , the relative standard deviation of each element,  $\hat{\sigma}_i$ , where

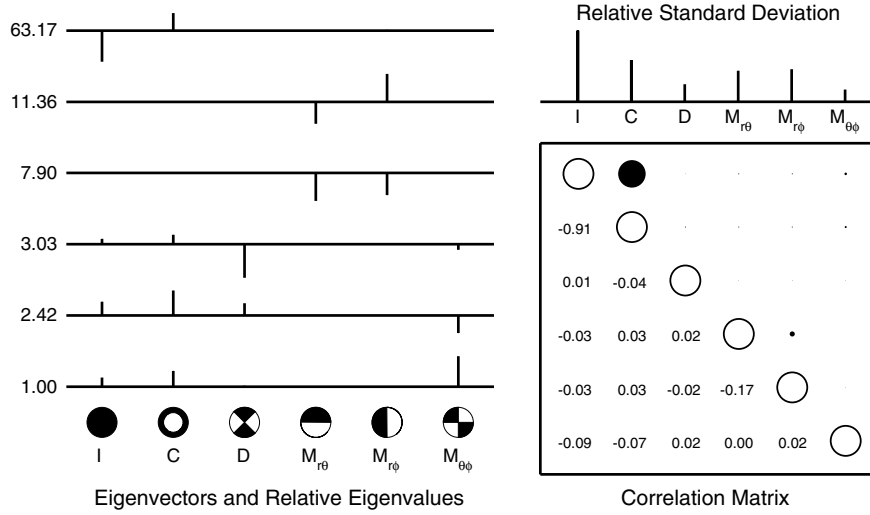


**Figure 5.** Results of an examination of the covariance matrix for the  $M_W$  5.6 vertical-P earthquake that occurred at Miyakejima volcano on 2 August 2000. On the left, we plot eigensolutions for  $\mathbf{A}^{-1}$ . Vertical lines in each row indicate the contributions of moment-tensor elements for each eigenvector, whose relative eigenvalue is given on the left. Positive contributions are plotted above the horizontal lines in each row, and negative contributions are plotted below. The eigenvectors are ordered by decreasing relative eigenvalue such that the top eigenvector shows the combination of moment-tensor elements that is the least well constrained. Focal mechanisms for the six elements of the moment tensor are plotted below the eigenvectors. On the right, we plot the relative standard deviations of the moment-tensor elements and the correlation matrix. In the correlation matrix, the moment-tensor elements are ordered ( $I$ ,  $C$ ,  $D$ ,  $M_{r\theta}$ ,  $M_{r\phi}$ ,  $M_{\theta\phi}$ ). The size and color of the circles plotted in the upper right of the correlation matrix represent the magnitude and sign of the correlation coefficients, which are printed in the bottom left of the correlation matrix. White circles indicate positive correlation coefficients, and black circles indicate negative correlation coefficients.

$$\hat{\sigma}_i = \sqrt{A_{ii}^{-1}} / \sigma_{\max} \quad (7)$$

and  $\sigma_i = \sqrt{A_{ii}^{-1}}$ , and the correlation matrix,  $\mathbf{X}$ , where

$$X_{ij} = A_{ij}^{-1} / \sigma_i \sigma_j. \quad (8)$$

[28] As illustrated in Figure 5, the least well-constrained eigenvector ( $-0.87I + 0.49C$ ) describes the isotropic and pure vertical-CLVD components of the moment tensor. These components have the largest relative standard deviations in addition to having a correlation coefficient of  $X_{IC} = -0.91$ , which demonstrates strong linear dependence. Other combinations of the moment-tensor elements have small-to-negligible correlation coefficients. These pieces of information underscore the fact that even for the best-recorded earthquakes in our data set, the isotropic and pure vertical-CLVD components of the moment tensor cannot be independently resolved using long-period seismic data.

[29] To explore the trade-off between the isotropic and pure vertical-CLVD components further, we calculate full moment-tensor solutions for the 86 vertical-CLVD earthquakes reported in Paper 1. We use the same data selections as in the preferred CMT analysis but allow for six independent elements of the moment tensor. With the additional free parameter, full moment tensor solutions provide slightly better fits to the data, improving the variance reduction by 1% on average.

[30] We decompose the full moment tensor,  $\mathbf{M}$ , into isotropic and deviatoric ( $\mathbf{M}'$ ) components, where

$$M'_{ij} = M_{ij} - \frac{1}{3}(M_{rr} + M_{\theta\theta} + M_{\phi\phi})\delta_{ij}. \quad (9)$$

[31] We define the isotropic moment,  $M_{\text{ISO}}$ , as

$$M_{\text{ISO}} = \frac{1}{3}(M_{rr} + M_{\theta\theta} + M_{\phi\phi}), \quad (10)$$

and the deviatoric moment,  $M_{\text{DEV}}$ , as

$$M_{\text{DEV}} = \frac{1}{2}(\lambda'_1 - \lambda'_3), \quad (11)$$

where  $\lambda'_1$  and  $\lambda'_3$  are the maximum and minimum eigenvalues of  $\mathbf{M}'$ . We also describe each earthquake in terms of two quantities,  $\varepsilon$ , which describes the non-double-couple contribution to the deviatoric moment tensor, and  $k$ , which describes the relative contributions of the isotropic and deviatoric components. We define  $k$  as

$$k = \frac{M_{\text{ISO}}}{|M_{\text{ISO}}| + M_{\text{DEV}}}. \quad (12)$$

[32] Because we follow GCMT convention to define the deviatoric moment, our definition of  $k$  differs slightly from that given by Hudson *et al.* [1989].

[33] In the left panel of Figure 6, we plot the deviatoric focal mechanisms ( $\mathbf{M}'$ ) for each earthquake on axes corresponding to the  $k$  and  $\varepsilon$  values of the full moment-tensor solutions. Moment tensors for earthquakes with explosive and implosive components have positive and negative  $k$

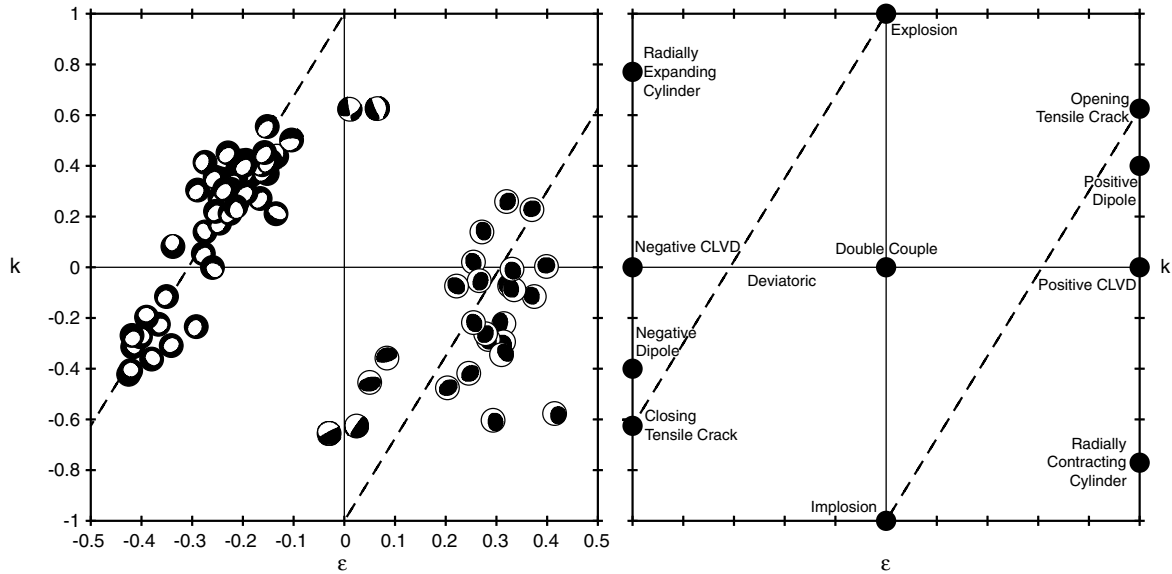


**Figure 6.** At left, we plot focal mechanisms for the deviatoric fraction of the full moment-tensor solutions for the 86 vertical-CLVD earthquakes analyzed here according to their  $k$  and  $\varepsilon$  values. On the right, we plot the locations of a variety of end-member seismic sources in  $k$ - $\varepsilon$  space. Dashed lines in both panels illustrate the trade-off between isotropic and vertical-CLVD components. See text for details.

values, respectively, and moment tensors for earthquakes with no net volume change plot along the line  $k=0$ . In the right panel, we provide a key to illustrate the  $k$  and  $\varepsilon$  values of end-member sources such as double-couple earthquakes, pure implosions and explosions, positive and negative CLVDs, positive and negative dipoles, opening and closing tensile cracks, and radially expanding and contracting cylinders, assuming that the Lamé constants,  $\lambda$  and  $\mu$ , are equal [Chouet, 1996; Kawakatsu and Yamamoto, 2007; Kumagai, 2009].

[34] We find that the full moment-tensor solutions for the vertical-CLVD earthquakes from Paper 1 plot roughly along two lines that span wide ranges of  $k$ - $\varepsilon$  space. Vertical-P earthquakes plot close to the line joining closing tensile cracks with pure explosions, and vertical-T earthquakes plot close to the line joining opening tensile cracks with pure implosions. Because the dominant principal stress axes are close to vertical, the focal mechanisms are consistent with tensile cracks oriented subhorizontally. Focal mechanisms for vertical positive and negative dipoles would also plot close to these lines.

[35] The dashed lines in Figure 6 are drawn for illustrative purposes based on visual inspection of the trends of the full moment-tensor solutions for vertical-CLVD earthquakes in  $k$ - $\varepsilon$  space. However, we also performed a numerical experiment for the  $M_w$  5.6 vertical-P earthquake described in Figure 5 to examine the impact of the trade-off between the isotropic and pure vertical-CLVD components on our full moment-tensor solutions. We began with the deviatoric moment tensor presented in Paper 1 and calculated a suite of additional moment tensors by adding combinations of the isotropic and pure vertical-CLVD components (equations (4) and (5)) in the proportions described by  $(-0.87I + 0.49C)$ , the eigenvector of the covariance matrix with the largest relative eigenvalue. We find an approximately linear relationship between the  $k$  and  $\varepsilon$  values for this suite of moment tensors extending from  $-0.55 < k < 0.55$

and  $-0.5 < \varepsilon < 0$ . The slope of this line is slightly lower than the dashed lines drawn in Figure 6 but approximates the observed trends of the full moment-tensor solutions for vertical-CLVD earthquakes well.

### 3. Discussion of Physical Mechanisms

[36] In this section, we examine the two main classes of physical mechanisms that have been proposed to explain vertical-CLVD earthquakes, mechanisms involving fluid flow and/or volumetric changes and ring-faulting mechanisms. We describe the proposed physical mechanisms and evaluate them using the constraints and understanding developed in Paper 1 and section 2. We use published results from field geology and analog and numerical models as further constraints on physical parameters such as the propagation velocity of fluid-filled tensile cracks and the geometry of ring faults. Because we cannot constrain the relative contributions of the isotropic and pure vertical-CLVD components in our waveform inversions, we do not interpret individual full moment-tensor solutions. Instead, we choose to interpret the range of potential mechanisms allowed by the solution space for the full data set of earthquakes.

[37] Key constraints that can be used to evaluate potential physical mechanisms for producing vertical-CLVD earthquakes include the following: First, vertical-CLVD earthquakes have slower source processes than tectonic earthquakes of the same magnitude, and vertical-P earthquakes appear to have slower source processes than vertical-T earthquakes. Vertical-T earthquakes have durations of  $\sim 10$  s or less, whereas vertical-P earthquakes can have durations as long as  $\sim 60$  s. Second, vertical-P earthquakes typically occur after volcanic eruptions or the start of volcanic unrest, whereas vertical-T earthquakes most often occur beforehand. Third, although seismic radiation

from vertical-CLVD earthquakes is dominated by Rayleigh waves radiated in approximately equal amplitude in all directions, we do observe small-amplitude Love waves for many events. As demonstrated in Figure 2, *SH* waves are also observed for many vertical-CLVD earthquakes. Fourth, there appears to be an upper limit on the source size of vertical-CLVD earthquakes, with no events larger than  $M_W$  5.8 observed. Finally, vertical-CLVD earthquakes are most commonly associated with volcanoes that erupt basaltic and/or andesitic lavas, as well as volcanoes that have calderas. We search for physically plausible mechanisms that can explain these observations.

### 3.1. Fluid-Transport and Volumetric-Change Mechanisms

[38] In volcano seismology, small earthquakes are routinely attributed to sources with net volume changes. Common sources associated with magma or fluid transport include spherical isotropic sources, opening or closing tensile cracks, and radially expanding or contracting cylinders (Figure 6) [Chouet, 1996; Kawakatsu and Yamamoto, 2007; Kumagai, 2009]. The moment tensors for volume-change mechanisms of these end-member reservoir types are well defined [Kawakatsu and Yamamoto, 2007], and we describe them briefly here. In each case,  $\Delta V$  is the stress-free volumetric strain that characterizes the amount of fluid that is injected or withdrawn from the reservoir [Aki and Richards, 2002]. Due to the confining pressure of the medium and the geometry of the reservoir, the actual volume change of the reservoir, the Mogi volume  $\Delta V_m$ , may be smaller than  $\Delta V$  [Richards and Kim, 2005; Kawakatsu and Yamamoto, 2007].

[39] In standard spherical coordinates ( $r$ ,  $\theta$ ,  $\phi$ ), the moment tensor for a spherical reservoir is given by

$$M_{\text{sphere}} = \Delta V \begin{bmatrix} \lambda + \frac{2}{3}\mu & 0 & 0 \\ 0 & \lambda + \frac{2}{3}\mu & 0 \\ 0 & 0 & \lambda + \frac{2}{3}\mu \end{bmatrix}, \quad (13)$$

where

$$\frac{\Delta V_m}{\Delta V} = \frac{\lambda + (2/3)\mu}{\lambda + 2\mu}. \quad (14)$$

[40] The moment tensor corresponding to a horizontal tensile crack that opens or closes vertically is

$$M_{\text{crack}} = \Delta V \begin{bmatrix} \lambda + 2\mu & 0 & 0 \\ 0 & \lambda & 0 \\ 0 & 0 & \lambda \end{bmatrix}. \quad (15)$$

[41] In this case,

$$\Delta V = \Delta V_m = S\Delta\bar{u}, \quad (16)$$

where  $S$  is the crack area and  $\Delta\bar{u}$  is the crack opening or closing width.

[42] The moment tensor corresponding to the radial expansion of a cylinder with a vertical symmetry axis is

$$M_{\text{cylinder}} = \Delta V \begin{bmatrix} \lambda & 0 & 0 \\ 0 & \lambda + \mu & 0 \\ 0 & 0 & \lambda + \mu \end{bmatrix}, \quad (17)$$

where

$$\frac{\Delta V_m}{\Delta V} = \frac{\lambda + \mu}{\lambda + 2\mu}. \quad (18)$$

[43] By applying a rotation matrix to equations (15) and (17), we can obtain moment tensors for tensile cracks or cylindrical sources of any orientation. Below, we consider a variety of fluid-transport and volumetric-change mechanisms, and compare them to our observations.

#### 3.1.1. Volume Exchange

[44] During rapid fluid transport, seismic sources with CLVD moment tensors can be produced by the contraction of one reservoir and the simultaneous, volume-compensated expansion of another. Vertical-CLVD earthquakes can be produced by mass or volume exchange between specific types and orientations of reservoirs. For example, pure vertical-P moment tensors can be produced by the transport of fluid from a horizontal tensile crack into a vertical cylinder. Likewise, pure vertical-T moment tensors can be produced by fluid flow from a vertical cylinder into a horizontal tensile crack [Chouet, 1996]. Vertical-CLVD moment tensors can also be produced by volume exchange between reservoirs that are not perfectly spherical, cylindrical or planar. In these cases, the radiation pattern of Rayleigh waves is not azimuthally isotropic and *SH* and Love waves are produced. Theoretically, larger vertical-CLVD earthquakes should be produced when greater amounts of mass or volume are exchanged between two reservoirs. Likewise, the frequency content of the earthquakes caused by mass- or volume-exchange processes should be influenced by the duration of the exchange process, such that longer exchanges produce slower, lower frequency earthquakes. Our observations of vertical-CLVD earthquakes would suggest that specific volume exchange scenarios are favored pre-eruption and post-eruption, and that episodes of volume exchange take place at different rates.

[45] A volume-exchange process has been investigated as a way to explain the  $M_W$  5.6 vertical-T earthquake that occurred in Iceland prior to a subglacial eruption between Bárðarbunga and Grimsvötn volcanoes in September 1996. *Tkalčić et al.* [2009] calculated a full moment-tensor solution for this event using regional seismic data and found it to have a statistically insignificant isotropic component, which they attempted to replicate by modeling volume exchange between two magma chambers separated by varying vertical distances. After calculating moment tensors for synthetic data generated by various configurations of inflating and deflating magma chambers with full volume compensation, *Tkalčić et al.* [2009] concluded that a mass-exchange mechanism is likely to result in a statistically significant observed isotropic component, even using long-period seismic data.

[46] The volume-exchange mechanism is unlikely to explain the Bárðarbunga earthquake, and we consider it an unlikely mechanism to explain most vertical-CLVD earthquakes because it requires very special conditions. Very low-viscosity fluids are required for rapid volume exchange, and as we discuss below, the volumes of fluids and the rates

of fluid flow that would be required to generate vertical-CLVD earthquakes with the observed magnitudes and source durations are extremely large. It is not obvious why rapid volume exchange should take place at volcanoes with caldera structures or at volcanoes located in specific geodynamic settings. Similarly, unless the source volcanoes are preferentially associated with small magma chambers, it is not clear why the volume of fluid that can be exchanged between two reservoirs should be limited. We therefore consider volume-exchange mechanisms an unlikely source for the vertical-CLVD earthquakes we observe. Below, we consider mechanisms that do not require volume compensation.

### 3.1.2. Tensile Cracks

[47] In volcanic and geothermal areas, at depths of up to several km, high fluid pressure can force open tensile cracks, generating earthquakes with unusual seismic radiation patterns. In addition to producing  $P$  waves with first motions of a single polarity, perfectly horizontal tensile cracks excite no  $SH$  or Love waves and radiate Rayleigh waves with equal amplitude in all directions. Small-amplitude  $SH$  and Love waves are radiated by subhorizontal tensile cracks, which open or close at shallow angles.

[48] As illustrated in Figure 6, earthquakes with deviatoric vertical-CLVD moment tensors can be produced by subhorizontal tensile cracks. Vertical-T earthquakes, which generally occur before volcanic eruptions, are consistent with opening tensile cracks, and vertical-P earthquakes, which generally occur after the start of volcanic unrest, are consistent with closing tensile cracks. If vertical-CLVD earthquakes can be explained by such a mechanism, our observation that vertical-P earthquakes have longer source durations than vertical-T earthquakes would suggest that the process of opening subhorizontal tensile cracks is faster than the process of closing them. The magnitude distributions of vertical-CLVD earthquakes in Figure 4 would also suggest that a limited volume of fluid can be emplaced in tensile cracks, at least on seismogenic timescales. Below, we evaluate the tensile-crack mechanism by considering the fluid volumes and propagation velocities required to generate the vertical-CLVD earthquakes reported in Paper 1.

[49] The magnitude of an earthquake generated by the opening or closing of a tensile crack is dependent on the elastic properties of the surrounding matrix and the volume of emplaced fluid. An estimate of the fluid volumes required by our observations of vertical-CLVD earthquakes can be calculated using the range of scalar moments presented in Paper 1,  $3.8 \times 10^{15}$  Nm to  $6.5 \times 10^{17}$  Nm. Assuming  $\lambda = \mu = 3.0 \times 10^{10}$  N/m<sup>2</sup> and using equations (15) and (16), the vertical-CLVD earthquakes from Paper 1 are consistent with subhorizontal tensile cracks with Mogi volumes ranging from  $\sim 5 \times 10^4$  m<sup>3</sup> to  $\sim 8 \times 10^6$  m<sup>3</sup>. These volumes are equivalent to square tensile cracks with side lengths of  $\sim 200$  m to  $\sim 3$  km and widths of 1 m.

[50] Generally, it is assumed that fluid-driven tensile cracks cannot propagate faster than fluid can flow following the crack tip. Among other factors, the propagation velocity of tensile cracks is limited by the viscosity of the fluid and the width of the crack. Magmatic intrusions propagate at velocities on the order of 0.01 to 10 m/s [Rubin, 1995], which are far too slow to radiate seismic waves. However, tensile cracks driven by less viscous hydrothermal fluids can propagate fast enough to generate seismic waves [Miller et al., 1998b; Ross et al., 1996; Foulger et al., 2004].

[51] Some authors have explained  $M_W > 4.5$  non-double-couple earthquakes at Long Valley Caldera [Dreger et al., 2000; Templeton and Dreger, 2006; Minson and Dreger, 2008], Bárðarbunga [Konstantinou et al., 2003], and Smith Rock volcanoes [Kanamori et al., 1993] by mechanisms involving tensile failure due to the injection of high-pressure, non-magmatic fluids.

[52] Under certain conditions, it may be possible for tensile cracks to generate earthquakes provided they can propagate ahead of the driving fluid at elastic wave speeds. It has been suggested that tensile cracks may propagate unstably when they emanate from magma chambers or when they approach the free surface or other tensile cracks [Sammis and Julian, 1987]. Three  $M_W > 5$  non-double-couple earthquakes at Long Valley Caldera have been attributed to unstable dike propagation [Julian, 1983; Aki, 1984; Julian and Sipkin, 1985], although this interpretation remains controversial [Ekström and Dziewonski, 1983]. Given that vertical-T earthquakes have source dimensions of at least several hundred meters and source-time functions ranging from a few seconds to a few tens of seconds, our observations would require propagation velocities of at least  $\sim 100$  m/s. Even though most volcanoes associated with vertical-T earthquakes erupt low-viscosity magmas, some special condition would be required to explain these events by the opening of magma-filled tensile cracks. It is not clear why such a mechanism would be linked to specific volcanic and geodynamic settings.

[53] Although fluid-driven tensile cracks may be able to open rapidly under some circumstances, they are generally expected to close slowly and not radiate seismic waves [Julian et al., 1998]. However, mine collapse, which is the rapid closing of air-filled cavities, has produced earthquakes with full moment tensors closely resembling closing horizontal tensile cracks [Pechmann et al., 1995; Bowers and Walter, 2002; Ford et al., 2008; Pechmann et al., 2008], some with magnitudes up to  $M \sim 5$  [Knoll, 1990; Pechmann et al., 1995; Gibowicz and Lasocki, 2001]. At shallow depths, a moment tensor representing a closing horizontal tensile crack [Day and McLaughlin, 1991; Bowers and Walter, 2002] produces approximately the same waveforms as a vertical single force representing the downward motion of a crustal block [Taylor, 1994]. Below, we consider this mechanism for the special case of caldera collapse.

[54] Over a  $\sim 40$  day period in the summer of 2000, the summit caldera of Miyakejima volcano in Japan subsided incrementally. Each discrete collapse episode produced tilt steps and very-long-period (VLP) earthquakes [Kikuchi et al., 2001; Kumagai et al., 2001; Ukawa et al., 2000; Yamamoto et al., 2001] that correlate strongly with changes in the caldera volume [Michon et al., 2011]. As described in Paper 1, the caldera collapse of Miyakejima also produced 43 earthquakes with deviatoric vertical-P moment tensors, the majority of which are directly associated with tilt steps and VLP earthquakes. The combined scalar moment of the vertical-P earthquakes is  $\sim 5.1 \times 10^{18}$  Nm, which is consistent with a closing tensile crack of volume  $\sim 6.4 \times 10^7$  m<sup>3</sup>. Because the final volume of the caldera is nearly 10 times larger,  $\sim 6 \times 10^8$  m<sup>3</sup> [Geshi et al., 2002; Nakada et al., 2005], a source model resembling a closing horizontal tensile crack is unlikely to fully explain the vertical-P earthquakes at Miyakejima. However, because  $\lambda$  may be

significantly lower than  $3.0 \times 10^{10}$  N/m<sup>2</sup> in volcanic environments [Rubin and Pollard, 1987], we cannot exclude the possibility that a source process resembling a closing tensile crack contributes to the seismic wavefield associated with caldera-collapse earthquakes.

[55] The opening and closing of tensile cracks is a physical mechanism that is most plausible for small earthquakes with depths in the upper few hundred meters of the crust. Due to the large overburden, very high fluid pressures are required to open tensile cracks at greater depths [Rubin, 1995]. From teleseismic body-wave modeling, we know that some vertical-CLVD earthquakes have focal depths of  $\sim 4\text{--}8$  km. Given the magnitudes, depths and source durations of vertical-CLVD earthquakes, we consider the opening and closing of tensile cracks to be an unlikely physical mechanism.

### 3.1.3. Other Types of Volumetric Changes

[56] In addition to tensile cracks, which are relatively thin and planar [Rubin, 1995], rapid volumetric changes in reservoirs with other shapes can produce seismic signals with deviatoric vertical-CLVD moment tensors. If the deforming reservoir has a sill-like or oblate ellipsoidal shape, the seismic radiation pattern will resemble a subhorizontal tensile crack [Davis, 1986; Fialko et al., 2001; Amoroso and Crescentini, 2009], and if the deforming reservoir is approximately spherical, the seismic radiation pattern will resemble an isotropic source. Although it is not immediately obvious why the expansion and contraction of reservoirs should occur at different rates, or why the volume of fluid injected or withdrawn should be limited, we consider both sill-like and spherical sources.

[57] We consider the rapid expansion or contraction of a sill-like magma chamber to be an unlikely mechanism for most vertical-CLVD earthquakes due to the large volume fluxes that would be required to explain the observed magnitudes and source durations. For example, the  $M_W$  5.8 vertical-T earthquake that took place in the Kermadec Islands on 17 February 2009 has a source duration of  $\sim 8$  s (Table 1). A volume change of  $\sim 8 \times 10^6$  m<sup>3</sup> and, therefore, a volume flux of  $\sim 1 \times 10^6$  m<sup>3</sup>/s would be required to explain this earthquake using a physical mechanism consisting of an opening magma-filled tensile crack. This estimate for the magma volume flux exceeds the estimated mass eruption rates for Pinatubo and Tambora volcanoes [Self, 2012] and several flood-basalt eruptions [Self et al., 1998]. It is possible that some vertical-CLVD earthquakes are generated by volumetric changes of sill-like reservoirs filled with non-magmatic fluids. High-pressure hydrothermal fluids such as water or carbon dioxide have lower viscosities that would be consistent with faster volume fluxes. However, it is not clear why the injection or withdrawal of hydrothermal fluids should occur preferentially at volcanoes with low silica content, or at volcanoes with caldera structures.

[58] Considering spherical sources, as illustrated in Figure 6, vertical-P earthquakes are consistent with explosions, and vertical-T earthquakes are consistent with implosions. Assuming  $\lambda = \mu = 3.0 \times 10^{10}$  N/m<sup>2</sup> and using equations (13) and (14), we estimate the isotropic volume changes that would be required to generate vertical-CLVD earthquakes with our observed range of scalar moments  $3.8 \times 10^{15}$  Nm– $6.5 \times 10^{17}$  Nm. The magnitudes of our vertical-CLVD earthquakes are consistent with volumes ranging from  $\sim 4 \times 10^4$  m<sup>3</sup> to  $\sim 7 \times 10^6$  m<sup>3</sup>, which is

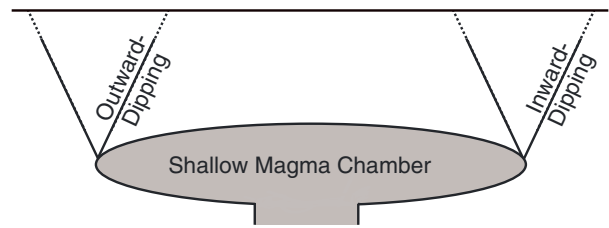


**Figure 7.** Schematic diagram for inward- and outward-dipping ring faults located above a shallow magma chamber. The ring faults are cone shaped in three dimensions. Dashed lines indicate that the ring faults may terminate below the surface.

equivalent to spherical sources with radii between  $\sim 20$  m and  $\sim 120$  m.

[59] Isotropic source mechanisms would require large volume fluxes, and in order to explain the frequency content of the vertical-CLVD earthquakes, implosive processes would have to be faster than explosive processes. Because we cannot explain why this process should be associated with specific types of volcanoes or geodynamic settings, and since we believe it is unlikely that implosive processes would precede volcanic eruptions and explosive processes follow, we consider isotropic source mechanisms unlikely to explain vertical-CLVD earthquakes.

## 3.2. Ring-Faulting Mechanisms

[60] Ring faults are curved or cone-shaped dip-slip faults that are circular to elliptical in plan view (Figure 7). These faults are formed by the inflation and deflation of shallow magma chambers and are associated caldera collapse and resurgence [Gottsmann and Marti, 2008, and references therein]. Although ring faults are inherently difficult to observe because they are often covered by lava, pyroclastic flow deposits, or crater lakes, both inward- and outward-dipping ring faults have been mapped at eroded volcanoes [e.g., Lipman, 1997; Cole et al., 2005; Geyer and Marti, 2008]. At volcanoes such as Rabaul [Mori and McKee, 1987], Pinatubo [Mori et al., 1996], Mt. Spurr [Jolly et al., 1994], Mt. St. Helens [Scandone and Malone, 1985], Mammoth Mountain in Long Valley Caldera [Prejean et al., 2003], and Mauna Kea [Wolfe et al., 2004], the presence of ring faults has been inferred from circular or elliptical patterns in microseismicity. Most ring faults are believed to have steep, approximately subvertical, dip angles [Gudmundsson and Nilsen, 2006, and references therein], although in analog models of caldera collapse [e.g., Roche et al., 2000; Acocella, 2008, and references therein], ring faults are often subvertical at depth and more shallowly dipping near the surface.

[61] Ring-faulting earthquakes may be expected to have lower rupture velocities, and therefore slower source processes, than standard tectonic earthquakes for several reasons. First, the velocity of rupture propagation during an earthquake is limited by the shear modulus of fault rocks. At volcanoes, the effective shear modulus of near-surface, fractured basalt is significantly lower than laboratory values [Rubin and Pollard, 1987], and as a result, the rupture velocity is low [e.g., Harrington and Brodsky, 2007]. The rupture velocity along ring faults may also be affected by unusual frictional and mechanical properties associated with

hydrothermal circulation, magmatic intrusions, high temperatures, and the effects of repeated collapse events. Finally, ring faults may have complicated geometries composed of several approximately planar fault segments instead of one smooth cone-shaped fault surface. Rupture velocity is known to decrease near regions of slip transfer from one fault segment to the next [e.g., *Wald and Heaton, 1994*].

[62] Dip-slip motion on ring faults can produce earthquakes with vertical-CLVD focal mechanisms. Slip on curved normal faults can produce vertical-P earthquakes, whereas slip on curved reverse ring faults can produce vertical-T earthquakes [*Ekström, 1994*]. The source parameters of these ring-faulting earthquakes will depend on the geometry and kinematics of the ring fault, as well as the scale and speed of rupture. Since vertical-T earthquakes have shorter source durations and generally occur before the start of volcanic unrest, whereas vertical-P earthquakes have longer source durations and generally occur afterwards, this would imply that the inflation of shallow magma chambers produces reverse ring-faulting earthquakes that have faster rupture velocities than the normal ring-faulting earthquakes produced by deflation processes.

[63] Because long-period seismic radiation patterns depend only on the final distribution of slip along a fault, we can approximate the moment tensors of reverse and normal ring-faulting earthquakes by summing the contributions of moment tensors for planar faults with constant dip and smoothly varying strike angles. Similar to the approach taken by *Ekström* [1994], we calculate hypothetical moment tensors for ring-faulting earthquakes following Box 4.4 of *Aki and Richards* [2002]. Fixing the rake to  $\pm 90^\circ$  for constant dip angles ranging from  $45^\circ$  to  $90^\circ$ , we vary the strike angles from  $0^\circ$  to  $360^\circ$  to simulate earthquakes rupturing different arc angles of a conical ring fault. For each combination of ring-fault dip and arc angle, we calculate the value of  $\varepsilon$ , the plunge of the dominant pressure or tension axis, and the normalized scalar moment, which is the ratio between the scalar moment of the composite moment tensor and the sum of the scalar moments for individual subfaults (Figure 8). Except for sources symmetric about a vertical axis, which are produced when the entire arc of the ring fault is ruptured in a single earthquake, small-amplitude *SH* and Love waves will be generated.

[64] The value of  $|\varepsilon|$  is largely controlled by the arc angle of the ring fault, whereas the plunge of the dominant principal stress axis is largely controlled by the dip angle of the ring fault. Earthquakes that rupture small portions of a ring fault are approximately double couple, and in general, earthquakes that rupture greater arc angles have higher non-double-couple components. However, for ruptures extending past  $\sim 180^\circ$  of arc, the non-double-couple component does not always increase with arc angle. For equal arc angles, earthquakes on more steeply dipping ring faults have dominant principal stress axes with shallower plunges. Earthquakes that rupture the entire circumference of a ring fault are pure vertical-CLVD events with  $\varepsilon = \pm 0.5$  and dominant vertical pressure or tension axes.

[65] As demonstrated in the bottom panel of Figure 8, dip-slip motion on ring-fault structures also results in the partial cancellation of seismically radiated long-period moment. For many combinations of dip and arc angles, the sum of the scalar moments (product of shear modulus, fault area, and

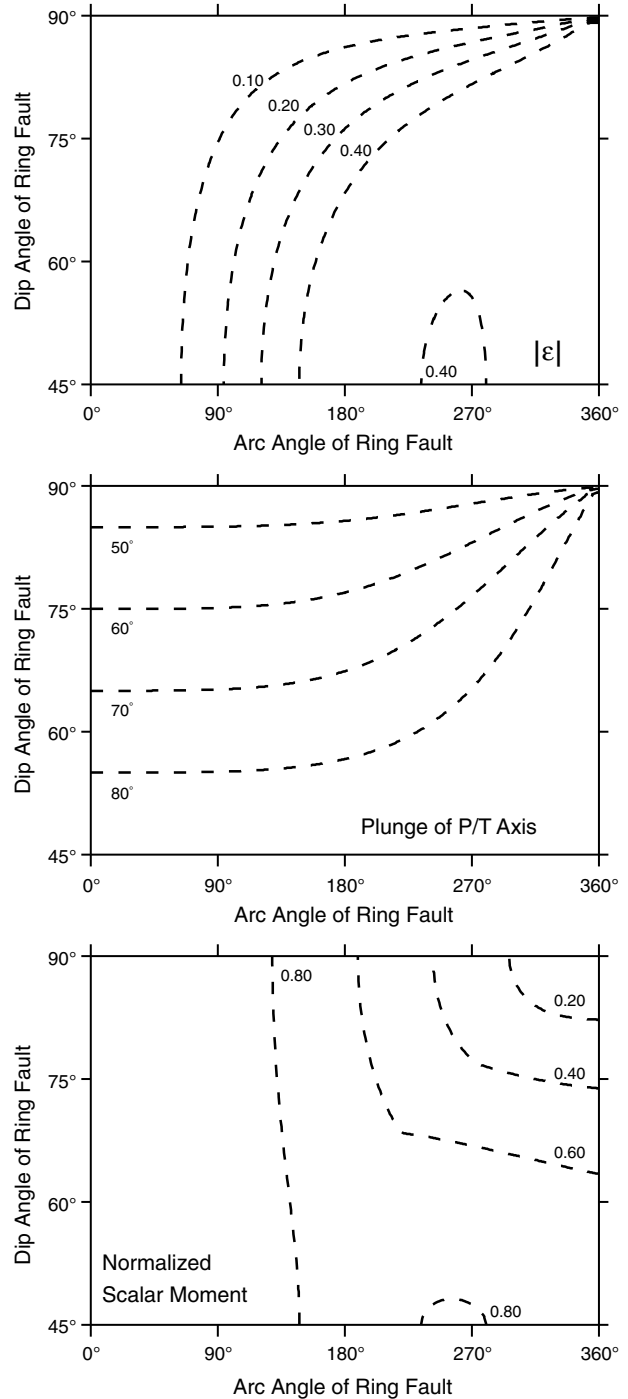


**Figure 8.** Source parameters for the composite moment tensors resulting from different slip distributions along cone-shaped ring faults. Ring-fault dip is plotted on the vertical axis and the ruptured arc angle on the horizontal axis. All simulated earthquakes are pure dip-slip events. The top panel shows  $|\varepsilon|$ , which represents the strength of the non-double-couple component of the composite moment tensor. The middle panel shows the plunge of the dominant principal stress axis. The bottom panel shows the normalized scalar moment, which is the ratio between the scalar moment for the composite moment tensor and the sum of the scalar moments for individual subfaults.

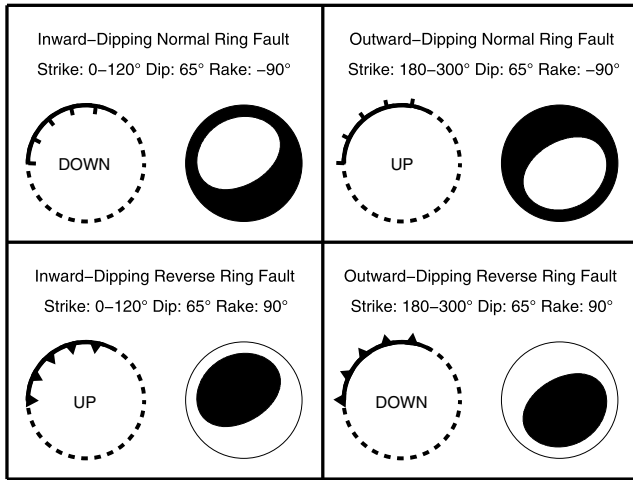


**Figure 9.** A comparison of the composite moment tensors that result from dip-slip motion along a fixed arc segment. In each quadrant, we plot a schematic indicating the dip direction of the ring fault (inward or outward) and the relative motion of the central crustal block (up or down) as well as the matching focal mechanism. Details of the fault parameters are listed at the top of each quadrant.

displacement) resulting from slip on individual subfaults will be larger than the scalar moment of the composite moment tensor determined by CMT analysis [Ekström, 1994]. Consequently, the actual displacement during a ring-faulting earthquake will be larger than expected from empirical relationships between average displacement and  $M_W$  like those developed by Wells and Coppersmith [1994]. In the end-member case, slip on a cylindrical fault surface will not produce any long-period seismic radiation. The partial cancellation of long-period seismic moment resulting from slip on ring-fault structures may partially account for vertical-CLVD earthquakes having longer-than-average source durations. It may also explain why vertical-T earthquakes near Smith Rock volcano are associated with disproportionately large tsunamis [Ekström, 1994].

[66] For any specified combination of dip and arc angles, the largest-magnitude vertical-CLVD earthquakes are expected to occur on ring faults with the largest dimensions, or in cases where vertical displacements along ring-fault systems are especially large. The fact that we do not observe any vertical-CLVD earthquakes with magnitudes larger than  $M_W$  5.8 could be due to the dimensions of ring faults at source volcanoes. Small calderas, and therefore small ring faults, are formed at volcanoes located in Mariana-type subduction zones or in oceanic crust, as well as at volcanoes that erupt tholeiitic or alkaline magmas, which are low in silica content [Sobradelo et al., 2010]. In Paper 1, we found that moderate-sized vertical-CLVD earthquakes most commonly occur at basaltic-to-andesitic stratovolcanoes and submarine volcanoes located in subduction zones, which suggests that vertical-CLVD earthquakes may be generated by dip-slip motion on relatively small ring-fault structures.

[67] If we consider a ring fault circumscribing a conical crustal block, four distinctly different moment tensors can be produced for the same dip and arc angles, depending on whether the ring fault dips inward or outward and whether

the central crustal block moves up or down relative to the rest of the volcano. In Figure 9, we show composite moment tensors for earthquakes generated by dip-slip motion along the same  $120^\circ$  of arc for ring faults dipping  $65^\circ$ . Following the convention of Aki and Richards [2002], in which the fault dips down to the right of the strike direction, we use strike angles varying between  $0^\circ$  and  $120^\circ$  for inward-dipping ring faults and strike angles varying between  $180^\circ$  and  $300^\circ$  for outward-dipping ring faults. We fix the rake to  $\pm 90^\circ$  to simulate pure normal and reverse ring-faulting earthquakes.

[68] As illustrated in Figure 9, for cases in which the ring fault is inward-dipping and the crustal block moves downward, either due to the deflation of an underlying magma chamber or the inflation of an overlying magma chamber, vertical-P earthquakes are produced. Vertical-T earthquakes are produced if the kinematics are reversed and the same crustal block moves upward due to the inflation of an underlying magma chamber. Similarly, the upward motion of an outward-dipping crustal block can produce vertical-P earthquakes, whereas the downward motion of the same crustal block produces vertical-T earthquakes. For inward-dipping ring faults, the azimuth of the dominant principal stress axis bisects the ring fault slip distribution, whereas for outward-dipping ring faults, the midpoint of the ruptured arc segment is offset by  $180^\circ$  from the azimuth of the dominant principal stress axis.

[69] If vertical-CLVD earthquakes are generated by slip on ring faults, deviatoric moment-tensor solutions should contain information about ring-fault geometry and the extent of rupture. In Figure 10, assuming rupture patterns can be approximated by uniform slip along a conical ring fault as in Figure 8, we use the values of  $\epsilon$  and the plunges of the dominant principal stress axes retrieved from the CMT solutions in Paper 1 to estimate the dip and arc angles of ring faults. For most vertical-CLVD earthquakes, these source parameters result in unique estimates. However, because the  $\epsilon$  patterns become complicated for ruptures extending past  $180^\circ$  of arc, the source parameters for a small number

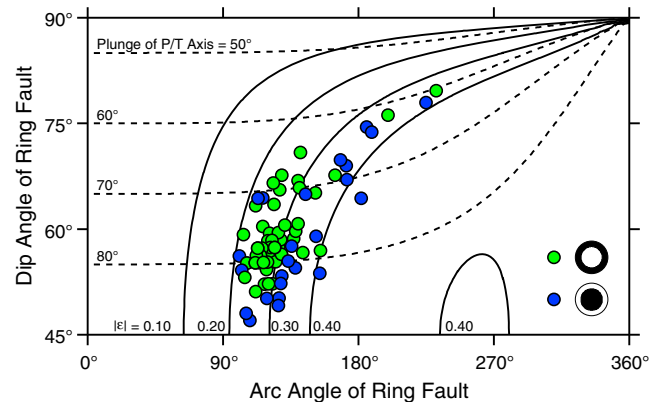


**Figure 10.** Application of the conical ring-faulting model from Figure 7 to the 86 vertical-CLVD earthquakes from Paper 1. We invert the values of  $|\epsilon|$  and the plunges of the dominant principal stress axes to obtain estimates of the dip and arc angles of ring faults. Green circles represent vertical-P earthquakes and blue circles represent vertical-T earthquakes. Black lines show contours of  $|\epsilon|$ , and dashed lines show contours of the plunge of the dominant pressure or tension axes.

of earthquakes with  $|\varepsilon| > 0.40$  are consistent with several possible combinations. For these earthquakes, we select solutions with the smallest arc angles in order to be consistent with the results for the majority of other earthquakes. We estimate that the uncertainties associated with the plunges of the dominant stress axes are on the order of  $5\text{--}10^\circ$ , and the uncertainties associated with the  $\varepsilon$  values are  $\sim 0.05\text{--}0.10$ , which translates to uncertainties of  $\sim 30^\circ$  in arc angle and  $\sim 10^\circ$  in dip angle.

[70] We find that the source parameters of the 86 vertical-CLVD earthquakes identified in Paper 1 are consistent with slip along  $\sim 100^\circ\text{--}250^\circ$  of arc on ring faults dipping  $45^\circ\text{--}80^\circ$ . The vast majority of vertical-CLVD earthquakes cluster between arc angles of  $100^\circ\text{--}160^\circ$  and dip angles of  $50^\circ\text{--}70^\circ$ , and we do not observe systematic differences between the ring-fault parameters estimated for vertical-P and vertical-T earthquakes. In cases where multiple vertical-CLVD earthquakes are associated with the same volcano, we find that the estimated ring-fault parameters are similar. For example, the 39 largest vertical-P earthquakes at Miyakejima have source parameters consistent with slip along  $\sim 110^\circ\text{--}125^\circ$  of arc on ring faults dipping  $\sim 55^\circ\text{--}60^\circ$ .

[71] The dip angles retrieved in Figure 10 are relatively shallow compared to the subvertical dip angles observed for ring faults in nature and in analog models. In fact, slip on subvertical ring faults should produce earthquakes with dominant principal stress axes that plunge  $45^\circ\text{--}60^\circ$ , which would not meet our criteria for being considered vertical-CLVD. Some of the steepest estimates of ring-fault dip are retrieved for vertical-T earthquakes at Sierra Negra and Rabaul, two volcanoes with known ring-fault structures. Although the estimates of ring-fault dip obtained from our CMT solutions are reasonably consistent with geophysical observations at these volcanoes, the relationship between inferred fault parameters and observed volcano deformation may not be simple in some cases.

[72] Sierra Negra is a shield volcano in the Galápagos Islands that began to erupt in October 2005 following an  $M_W$  5.5 vertical-T earthquake. The volcano is well known for the 14 km long C-shaped fault system contained in its summit caldera (Figure 11). This sinuous ridge is attributed to repeated episodes of asymmetrical uplift of the caldera floor driven by magma accumulation at shallow depths [Reynolds *et al.*, 1995; Amelung *et al.*, 2000; Jónsson *et al.*, 2005; Chadwick *et al.*, 2006; Jónsson, 2009]. Recently, deformation associated with trapdoor-faulting events has been explained by slip on curved and steeply inward-dipping ( $\sim 71^\circ$ ) thrust faults [Jónsson, 2009]. InSAR data suggest that the  $M_W$  5.5 vertical-T earthquake may be associated with a trapdoor-faulting event [Yun, 2007], an interpretation that is supported by vertical fault scarps measured along the sinuous ridge [Geist *et al.*, 2008].

[73] From the CMT analysis in Paper 1, the  $M_W$  5.5 vertical-T earthquake at Sierra Negra has an  $\varepsilon$  value of 0.37 and a tension axis that plunges  $62^\circ$ , which is consistent with dip-slip motion along  $\sim 220^\circ$  of arc on a ring fault dipping  $\sim 78^\circ$  (Figure 10). If the earthquake is associated with a trapdoor-faulting event, meaning it took place along the sinuous ridge on an inward-dipping reverse ring fault, the tension axis should plunge to the southwest. However, according to our CMT solution, which is A quality and well constrained, the tension axis has an azimuth of  $60^\circ$ ,

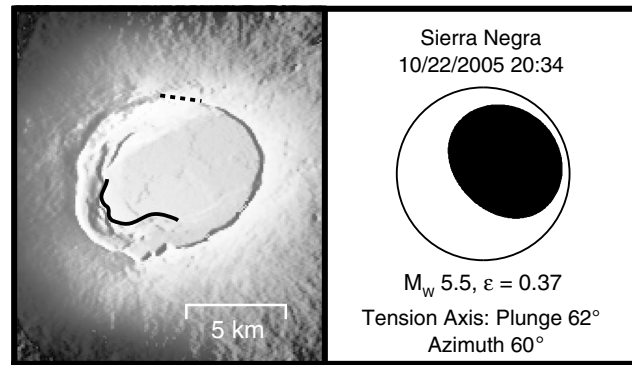


**Figure 11.** A map of the caldera of Sierra Negra volcano is plotted in the left panel. The dashed line indicates the location of the initial fissure for the 2005 eruption, and the black line indicates the location of the vertical fault scarp reported in Geist *et al.* [2008]. Topography is from the Shuttle Radar Topography Mission. The focal mechanism for the  $M_W$  5.5 vertical-T earthquake that occurred 3 h prior to the start of the 2005 eruption is plotted on the right.

consistent with uplift along an inward-dipping reverse ring fault in the northern and eastern regions of the caldera, or subsidence along an outward-dipping reverse ring fault in the southern and western regions of the caldera (Figure 9). These discrepancies may indicate that the surface geology [Geist *et al.*, 2008] and geodetic observations [Yun, 2007] do not directly reflect the deformation that occurred during the vertical-T earthquake. The earthquake may instead represent deformation at greater depths in the volcano.

[74] Four  $M_W$  5.0 vertical-T earthquakes took place at Rabaul volcano between 1991 and 1996. Rabaul is a pyroclastic shield volcano in Papua New Guinea where the locations of microearthquakes delineate a steeply outward-dipping ( $\sim 80^\circ$ ) elliptical ring fault extending to depths of 4–5 km [McKee *et al.*, 1984; Mori and McKee, 1987; Mori *et al.*, 1989; Itikarai, 2008 as referenced in Johnson *et al.*, 2010]. The first two vertical-T earthquakes took place during a period of caldera uplift prior to the 1994 eruption of Rabaul, which is a scenario that should produce vertical-P earthquakes provided the uplift is accommodated by slip on the observed outward-dipping ring fault (Figure 9). As at Sierra Negra, the vertical-T focal mechanisms for the Rabaul earthquakes are consistent with either subsidence of a caldera block bounded by an outward-dipping ring fault or uplift of a caldera block bounded by an inward-dipping ring fault. If the caldera uplift prior to the 1994 eruption was due to the inflation of a shallow magmatic or hydrothermal system [McKee *et al.*, 1984; Mori and McKee, 1987; Geyer and Gottsman, 2010], it is possible that the vertical-T earthquakes were caused by subsidence along the deeper outward-dipping ring fault. The vertical-T earthquakes could also have been caused by slip on antithetic inward-dipping ring-fault structures [Saunders, 2001, 2005].

[75] The ring-faulting model explains many characteristics of vertical-CLVD earthquakes, including their anomalous seismic radiation patterns, frequency content, and magnitudes. It also explains why we observe vertical-CLVD earthquakes at particular types of volcanoes. However, it remains difficult to relate observed earthquake source parameters to specific faulting scenarios. If the deviatoric moment-tensor

solutions for vertical-CLVD earthquakes are directly related to slip distributions on ring faults, these structures must have shallower dips than expected from field studies and analog models. On the other hand, if vertical-CLVD earthquakes are caused by slip on steeply dipping ring faults, the discrepancies between expected and observed source parameters must be explained. Small differences may be attributed to uncertainties in our CMT solutions. Larger differences could be the result of complexity associated with the ring-fault geometry or the rupture process. The discrepancies might also be explained in part by smaller contributions from unmodeled, non-zero isotropic components generated by the inflation or deflation of shallow magma chambers.

#### 4. Conclusions

[76] Moderate-sized vertical-CLVD earthquakes are some of the most anomalous earthquakes to occur in volcanic systems. In Paper 1, and *Nettles and Ekström* [1998] and *Shuler and Ekström* [2009], we identified 101 shallow vertical-CLVD earthquakes that occurred near active volcanoes. The majority of vertical-CLVD earthquakes are associated with basaltic and/or andesitic stratovolcanoes and submarine volcanoes located in subduction zones, although a small number of vertical-CLVD earthquakes are located in continental rifts, in areas of hotspot volcanism, and along mid-ocean ridges. Approximately 70% of vertical-CLVD earthquakes occur during episodes of volcanic unrest at nearby volcanoes, which suggests that these events are closely related to magma migration and eruption processes. Vertical-P earthquakes occur after the start of volcanic eruptions or episodes of unrest, whereas vertical-T earthquakes generally occur before volcanic eruptions.

[77] In this study, we performed additional analysis of the teleseismic body waves of  $5.1 \leq M_W \leq 5.8$  vertical-CLVD earthquakes and determined that these earthquakes have longer source durations than tectonic earthquakes of the same magnitude. We find that vertical-CLVD earthquakes from the GCMT catalog have source durations up to  $\sim 10$  s. We are unable to model any vertical-CLVD earthquakes detected only by analysis of surface waves [*Ekström*, 2006], but the inferred frequency content of those earthquakes suggests that they have even longer source durations, up to approximately 1 min [*Ohminato and Kumagai*, 2001]. Most vertical-CLVD earthquakes identified originally from the GCMT catalog are vertical-T events and most vertical-CLVD earthquakes from the Surface Wave catalog are vertical-P events, leading us to infer that vertical-P earthquakes may have slower source processes than vertical-T events. By examining the magnitude distributions of vertical-CLVD earthquakes, we also determined that there may be an upper limit for the source size of vertical-CLVD earthquakes, as we have observed  $\sim 75$  events with  $M_W \geq 5.0$  in the last  $\sim 35$  years, yet we have not observed any events larger than  $M_W$  5.8.

[78] Whereas previously we considered only deviatoric moment tensors, here we explored the possibility that vertical-CLVD earthquakes may have significant non-zero isotropic components generated by net volume changes. We examined the covariance matrix of one of the best-recorded vertical-CLVD earthquakes to illustrate that even for large earthquakes with excellent data coverage, there is a trade-off between the isotropic and pure vertical-CLVD

components of the moment tensor. As a result, many physical mechanisms might produce earthquakes with deviatoric vertical-CLVD moment tensors, including slip on ring faults, volume exchange between two reservoirs, the opening and closing of tensile cracks, and other types of volumetric changes. We used additional constraints obtained from our detailed studies of vertical-CLVD earthquakes to evaluate these proposed physical mechanisms.

[79] In general, physical mechanisms involving only fluid transport or volumetric changes are unlikely to explain vertical-CLVD earthquakes. Mechanisms involving isotropic volumetric changes cannot explain the temporal relationships between vertical-CLVD earthquakes and volcanic eruptions. Likewise, the source durations of vertical-CLVD earthquakes preclude mechanisms involving magma transport through tensile cracks. Even for basaltic or andesitic magmas, which have relatively low viscosities, the propagation velocities and volume fluxes required to explain our observations are physically implausible. It is possible that some vertical-CLVD earthquakes are caused by tensile cracks filled with less viscous hydrothermal fluids, such as water or carbon dioxide, although it is not clear why this mechanism should occur preferentially at basaltic stratovolcanoes and submarine volcanoes. In the special circumstance of caldera collapse, we cannot exclude the possibility that a mechanism resembling the closing of a subhorizontal tensile crack plays a role in producing some vertical-CLVD earthquakes.

[80] Ring-faulting mechanisms, on the other hand, can explain the anomalous seismic radiation patterns and source durations of vertical-CLVD earthquakes in addition to many of their other characteristics. The partial cancellation of long-period seismic moment that results from slip on curved fault structures can explain why vertical-CLVD earthquakes near Smith Rock volcano are associated with disproportionately large tsunamis. Additionally, ring-faulting mechanisms can explain why vertical-CLVD earthquakes are associated with particular types of volcanoes and tectonic settings. Most vertical-CLVD earthquakes are associated with basaltic-to-andesitic volcanoes with calderas that are located in oceanic island arcs. Calderas with small dimensions, and therefore ring faults with small dimensions, are preferentially observed at volcanoes in these environments [*Sobradelo et al.*, 2010], and basaltic volcanoes erupt more frequently than silicic volcanoes [*White et al.*, 2006]. The geodynamic environments of the source volcanoes may thus explain why no  $M_W > 6$  vertical-CLVD earthquakes have been observed to date.

[81] The deviatoric moment tensors of vertical-CLVD earthquakes are consistent with dip-slip motion on ring faults dipping  $\sim 50^\circ$ – $70^\circ$ . These estimates are shallow compared to the subvertical ring-fault dip angles inferred from field geology and analog models, but the dip angles of volcano ring faults are not well constrained. Field studies of active calderas cannot constrain deep structures, and it is not clear that the surface expressions of ring faults are representative of deeper seismogenic zones. Similarly, the inferred geometries of ring faults outlined by microseismicity are dependent on local velocity models and seismic station distributions. Additionally, numerical and analog models of caldera collapse are simplified, and in most cases, the effects of heterogeneity, pre-existing faults, and magma

intrusion and extrusion are not considered. Such factors may influence the stress field and affect the dip angles of the volcano ring faults. More work will be required to evaluate whether active volcanoes may have ring faults with shallower dip angles, consistent with our seismological observations.

[82] From our detailed studies of vertical-CLVD earthquakes, it is clear that these events are generated by large-scale deformation occurring inside the edifices and magmatic plumbing systems of active volcanoes. These earthquakes occur mainly in low-silica volcanic systems, and vertical-T earthquakes generally lead up to volcanic eruptions, whereas vertical-P earthquakes generally take place after the start of volcanic unrest. Our preferred physical mechanism for these events is dip-slip motion on ring faults, in which vertical-T earthquakes represent slip on curved reverse faults and vertical-P earthquakes represent slip on curved normal faults. It remains to be explained why inflation processes should trigger slip on reverse ring faults and deflation processes trigger slip on normal ring faults, and why earthquakes on reverse and normal ring faults appear to have different rupture velocities. In order to address these open questions, and to learn more about the specific deformation processes generating vertical-CLVD earthquakes at individual source volcanoes, it will be necessary to integrate teleseismic observations with data from multiparametric monitoring networks.

[83] **Acknowledgments.** We thank James B. Gaherty, William Menke, Cynthia J. Ebinger, Emily E. Brodsky, Editor Robert L. Nowack, and one anonymous reviewer for providing constructive comments that improved the manuscript. We are grateful to the IRIS Data Management Center for archiving and distributing the seismic data used in this study. This project was supported by National Science Foundation awards EAR-0944055 and EAR-0824694. AS was also supported by an NSF Graduate Research Fellowship.

## References

Acocella, V. (2008), Structural development of calderas: A synthesis from analog experiments, in *Caldera Volcanism: Analysis, Modelling and Response*, Developments in Volcanology, vol. 10, edited by J. Gottsman and J. Marti, pp. 285–311, Elsevier, Amsterdam.

Aki, K. (1984), Evidence for magma intrusion during the Mammoth Lakes earthquakes of May 1980 and implications of the absence of volcanic (harmonic) tremor, *J. Geophys. Res.*, *89*, 7689–7696.

Aki, K., and P. G. Richards (2002), *Quantitative Seismology*, 2nd ed., University Science Books, Sausalito, Calif.

Amelung, F., S. Jónsson, H. Zebker, and P. Segall (2000), Widespread uplift and “trapdoor” faulting on Galápagos volcanoes observed with radar interferometry, *Nature*, *407*, 993–996.

Amoruso, A., and L. Crescentini (2009), Shape and volume change of pressurized ellipsoidal cavities from deformation and seismic data, *J. Geophys. Res.*, *114*, B02210, doi:10.1029/2008JB005946.

Arvidsson, R., and G. Ekström (1998), Global CMT analysis of moderate earthquakes,  $M_w \geq 4.5$ , using intermediate-period surface waves, *Bull. Seism. Soc. Am.*, *88*(4), 1003–1013.

Bird, P. (2003), An updated digital model of plate boundaries, *Geochem. Geophys. Geosys.*, *4*(3), doi:10.1029/2001GC000252.

Bowers, D., and W. R. Walter (2002), Discriminating between large mine collapses and explosions using teleseismic P waves, *Pure Appl. Geophys.*, *159*, 803–830.

Chadwick, W. W., D. J. Geist, S. Jónsson, M. Poland, D. J. Johnson, and C. M. Meertens (2006), A volcano bursting at the seams: Inflating, faulting, and eruption at Sierra Negra volcano, Galápagos, *Geology*, *34*(12), 1025–1028, doi:10.1130/G22826A.1.

Chouet, B. A. (1996), New methods and future trends in seismological volcano monitoring, in *Monitoring and Mitigation of Volcano Hazards*, edited by R. Scarpa and R. I. Tilling, pp. 23–97, Springer-Verlag, Berlin.

Chouet, B., P. Dawson, T. Ohminato, M. Martini, G. Saccorotti, F. Giudicepietro, G. De Luca, G. Milana, and R. Scarpa (2003), Source mechanisms of explosions at Stromboli Volcano, Italy, determined from moment-tensor inversions of very-long-period data, *J. Geophys. Res.*, *108*(B1), 2019, doi:10.1029/2002JB001919.

Cole, J. W., D. M. Milner, and K. D. Spinks (2005), Calderas and caldera structures: A review, *Earth-Science Reviews*, *69*, 1–26.

D’Auria, L., F. Giudicepietro, M. Martini, and R. Peluso (2006), Seismological insights into the kinematics of the 5 April 2003 vulcanian explosion at Stromboli volcano (southern Italy), *Geophys. Res. Lett.*, *33*, L08308, doi:10.1029/2006GL026018.

Davis, P. M. (1986), Surface deformation due to inflation of an arbitrarily oriented triaxial ellipsoidal cavity in an elastic half-space, with reference to Kilauea Volcano, Hawaii, *J. Geophys. Res.*, *91*, 7429–7438.

Day, S. M., and K. L. McLaughlin (1991), Seismic source representations for spall, *Bull. Seism. Soc. Am.*, *81*(1), 191–201.

Dreger, D. S., H. Tkalčić, and M. Johnston (2000), Dilatational processes accompanying earthquakes in the Long Valley Caldera, *Science*, *228*(122), doi:10.1126/science.288.5463.122.

Dufumier, H., and L. Rivera (1997), On the resolution of the isotropic component in moment tensor inversion, *Geophys. J. Int.*, *131*, 595–606.

Dziewonski, A. M., T.-A. Chou, and J. H. Woodhouse (1981), Determination of earthquake source parameters from waveform data for studies of global and regional seismicity, *J. Geophys. Res.*, *86*(B4), 2825–2852.

Ekström, G. (1989), A very broad band inversion method for the recovery of earthquake source parameters, *Tectonophysics*, *166*, 73–100.

Ekström, G. (1994), Anomalous earthquakes on volcano ring-fault structures, *Earth Planet. Sci. Lett.*, *128*, 707–712.

Ekström, G. (2006), Global detection and location of seismic sources by using surface waves, *Bull. Seism. Soc. Am.*, *96*(4A), 1201–1212, doi:10.1785/0120050175.

Ekström, G., and A. M. Dziewonski (1983), Moment tensor solutions of Mammoth Lakes earthquakes (abstract), *Eos Trans. AGU*, *64*, 262.

Ekström, G., R. S. Stein, J. P. Eaton, and D. Eberhart-Phillips (1992), Seismicity and geometry of a 110-km-long blind thrust fault. 1. The 1985 Kettleman Hills, California, Earthquake, *J. Geophys. Res.*, *97*(B4), 4843–4864.

Ekström, G., M. Nettles, and A. M. Dziewonski (2012), The global CMT project 2004–2010: Centroid-moment tensors for 13,017 earthquakes, *Phys. Earth Planet. Inter.*, *200–201*, 1–9, doi:10.1016/j.pepi.2012.04.002.

Fialko, Y., Y. Khazan, and M. Simons (2001), Deformation due to a pressurized horizontal circular crack in an elastic half-space, with applications to volcano geodesy, *Geophys. J. Int.*, *146*, 181–190.

Filson, J., T. Simkin, and L.-K. Leu (1973), Seismicity of a Caldera Collapse: Galapagos Islands 1968, *J. Geophys. Res.*, *78*(35), 8591–8622.

Ford, S. R., D. S. Dreger, and W. R. Walter (2008), Source characterization of the 6 August 2007 Crandall Canyon mine seismic event in central Utah, *Seism. Res. Lett.*, *79*(5), 637–644, doi:10.1785/gssrl.79.5.637.

Foulger, G. R., B. R. Julian, D. P. Hill, A. M. Pitt, P. E. Malin, and E. Shalev (2004), Non-double-couple microearthquakes at Long Valley Caldera, California, provide evidence for hydraulic fracturing, *J. Volcanol. Geotherm. Res.*, *132*, 45–71.

Francis, T. J. G. (1974), A new interpretation of the 1968 Fernandina Caldera Collapse and its implications for the mid-oceanic ridges, *Geophys. J. R. Astr. Soc.*, *39*, 301–318.

Frohlich, C., and S. D. Davis (1993), Teleseismic *b* values: Or, much ado about 1.0, *J. Geophys. Res.*, *98*(B1), 631–644.

Geist, D. J., K. S. Harpp, T. R. Naumann, M. Poland, W. W. Chadwick, M. Hall, and E. Rader (2008), The 2005 eruption of Sierra Negra volcano, Galápagos, Ecuador, *Bull. Volcanol.*, *70*, 655–673, doi:10.1007/s00445-007-0160-3.

Geshi, N., T. Shimano, T. Chiba, and S. Nakada (2002), Caldera collapse during the 2000 eruption of Miyakejima Volcano, Japan, *Bull. Volcanol.*, *64*, 55–68, doi:10.1007/s00445-001-0184-z.

Geyer, A., and J. Gottsman (2010), The influence of mechanical stiffness on caldera deformation and implications for the 1971–1984 Rabaul uplift (Papua New Guinea), *Tectonophysics*, *483*, 399–412.

Geyer, A., and J. Marti (2008), The new worldwide collapse caldera database (CCDB): A tool for studying and understanding caldera processes, *J. Volcanol. Geotherm. Res.*, *175*, 334–354, doi:10.1016/j.jvolgeores.2008.03.017.

Gibowicz, S. J., and S. Lasocki (2001), Seismicity induced by mining: Ten years later, *Adv. Geophys.*, *44*, 39–181.

Gottsmann, J., and J. Marti (Eds) (2008), *Caldera Volcanism: Analysis, Modelling and Response*, Developments in Volcanology, vol. 10, Elsevier, Amsterdam, The Netherlands.

Gudmundsson, A., and K. Nilsen (2006), Ring-faults in composite volcanoes: structures, models and stress fields associated with their formation, in *Mechanisms of Activity and Unrest at Large Calderas*, Geological Society of London Special Pub., vol. 269, edited by C. Troise, G. De Natale, and C. R. J. Kilburn, pp. 83–108, Geological Society, London, U.K.

Gutenberg, B., and C. F. Richter (1944), Frequency of earthquakes in California, *Bull. Seism. Soc. Am.*, *34*, 185–188.

- Harrington, R. M., and E. E. Brodsky (2007), Volcanic hybrid earthquakes that are brittle-failure events, *Geophys. Res. Lett.*, *34*, L06308, doi:10.1029/2006GL028714.
- Hudson, J. A., R. G. Pearce, and R. M. Rogers (1989), Source type plot for inversion of the moment tensor, *J. Geophys. Res.*, *94*(B1), 765–774.
- Itikarai, I. (2008), The 3-D structure and earthquake locations at Rabaul Caldera, Papua New Guinea, unpublished Master of Philosophy thesis, 137 pp., Australian National University, Canberra.
- Johnson, R. W., I. Itikarai, H. Patia, and C. O. McKee (2010), Volcanic systems of the Northeastern Gazelle Peninsula, Papua New Guinea: Synopsis, evaluation, and a model for Rabaul Volcano, Papua New Guinea, *Rabaul Volcano Workshop Report*, Papua New Guinea Department of Mineral Policy and Geohazards Management, and Australian Agency for International Development, Port Moresby, Papua New Guinea.
- Jolly, A. D., R. A. Page, and J. A. Power (1994), Seismicity and stress in the vicinity of Mount Spurr volcano, south central Alaska, *J. Geophys. Res.*, *99*, 15,305–15,318.
- Jónsson, S. (2009), Stress interaction between magma accumulation and trapdoor faulting on Sierra Negra, Galápagos, *Tectonophysics*, *471*, 36–44.
- Jónsson, S., H. Zebker, and F. Amelung (2005), On trapdoor faulting at Sierra Negra volcano, Galápagos, *J. Volcanol. Geotherm. Res.*, *144*, 59–71.
- Julian, B. R. (1983), Evidence for dyke intrusion earthquake mechanisms near Long Valley Caldera, California, *Nature*, *303*, 323–325.
- Julian, B. R., and S. Sipkin (1985), Earthquake processes in the Long Valley Caldera area, California, *J. Geophys. Res.*, *90*, 11,155–11,169.
- Julian, B. R., A. D. Miller, and G. R. Foulger (1998), Non-double-couple earthquakes. 1. Theory, *Rev. Geophys.*, *36*(4), 525–549.
- Kanamori, H., and J. W. Given (1981), Use of long-period surface waves for rapid determination of earthquake source parameters, *Phys. Earth Planet. Inter.*, *27*, 8–31.
- Kanamori, H., G. Ekström, A. Dziewonski, J. S. Barker, and S. A. Sipkin (1993), Seismic radiation by magma injection: An anomalous seismic event near Tori Shima, Japan, *J. Geophys. Res.*, *98*(B4), 6511–6522.
- Kawakatsu, H. (1996), Observability of the isotropic component of a moment tensor, *Geophys. J. Int.*, *126*, 525–544.
- Kawakatsu, H., and M. Yamamoto (2007), Volcano seismology, in *Treatise on Geophysics*, vol. 4, edited by H. Kanamori, pp. 389–420, Elsevier, Amsterdam, doi:10.1016/B978-0-444-52748-6.00073-0.
- Kikuchi, M., Y. Yamanaka, and K. Koketsu (2001), Source process of the long-period seismic pulses associated with the 2000 eruption of Miyake-jima Volcano, and its implications (in Japanese with English abstract), *J. Geogr.*, *110*(2), 204–216.
- Knoll, P. (1990), The fluid-induced tectonic rockburst of March 13, 1989, in the “Werra” potash mining district of the GDR (first results), *Gerlands Beitrage zur Geophysik*, *99*, 29–245.
- Konstantinou, K. I., H. Kao, C. H. Lin, and W.-T. Liang (2003), Analysis of broad-band regional waveforms of the 1996 September 29 earthquake at Bárðarbunga volcano, central Iceland: Investigation of the magma injection hypothesis, *Geophys. J. Int.*, *154*, 134–145.
- Kumagai, H. (2009), Source quantification of volcano seismic signals, in *Encyclopedia of Complexity and Systems Science*, edited by R. A. Meyers, pp. 9899–9932, Springer, New York.
- Kumagai, H., T. Ohminato, M. Nakano, M. Ooi, A. Kubo, H. Inoue, and J. Oikawa (2001), Very-long-period seismic signals and caldera formation at Miyake Island, Japan, *Science*, *293*(5530), 687–690.
- Kumagai, H., M. Nakano, T. Maeda, et al. (2010), Broadband seismic monitoring of active volcanoes using deterministic and stochastic approaches, *J. Geophys. Res.*, *115*, B08303, doi:10.1029/2009JB006889.
- Lipman, P. W. (1997), Subsidence of ash-flow calderas: Relation to caldera size and magma-chamber geometry, *Bull. Volcanol.*, *59*, 198–218.
- McKee, C. O., P. L. Lowenstein, P. de Saint Ours, B. Talai, I. Itikarai, and J. J. Mori (1984), Seismic and ground deformation crises at Rabaul Caldera: Prelude to an eruption?, *Bull. Volcanol.*, *47*(2), 397–411.
- McNutt, S. R. (2000), Volcanic seismicity, in *Encyclopedia of Volcanoes*, edited by H. Sigurdsson, B. Houghton, S. R. McNutt, H. Rymer, and J. Stix, pp. 1015–1033, Academic Press, San Diego, Calif.
- McNutt, S. R. (2005), Volcanic seismology, *Annu. Rev. Earth Planet. Sci.*, *32*, 461–491, doi:10.1146/annurev.earth.33.092203.122459.
- Mendigüen, J. A., and K. Aki (1978), Source mechanism of the deep Colombian earthquake of 1970 July 31 from the free oscillation data, *Geophys. J. R. Astr. Soc.*, *55*, 539–556.
- Michon, L., F. Massin, V. Famin, V. Ferrazzini, and G. Roult (2011), Basaltic calderas: Collapse dynamics, edifice deformation, and variations of magma withdrawal, *J. Geophys. Res.*, *116*, B03209, doi:10.1029/2010JB007636.
- Miller, A. D., G. R. Foulger, and B. R. Julian (1998a), Non-double-couple earthquakes. 2. Observations, *Rev. Geophys.*, *36*(4), 551–568.
- Miller, A. D., B. R. Julian, and G. R. Foulger (1998b), Three-dimensional seismic structure and moment tensors of non-double-couple earthquakes at the Hengill-Grensadal volcanic complex, Iceland, *Geophys. J. Int.*, *133*, 309–325.
- Minson, S. E., and D. S. Dreger (2008), Stable inversions for complete moment tensors, *Geophys. J. Int.*, *174*, 585–592.
- Minson, S. E., D. S. Dreger, R. Bürgmann, H. Kanamori, and K. M. Larson (2007), Seismically and geodetically determined nondouble-couple source mechanisms from the 2000 Miyakejima volcanic earthquake swarm, *J. Geophys. Res.*, *112*, B10308, doi:10.1029/2006JB004847.
- Mori, J., and C. McKee (1987), Outward-dipping ring-fault structure at Rabaul Caldera as shown by earthquake locations, *Science*, *235*, 193–195.
- Mori, J., C. McKee, I. Itikarai, P. Lowenstein, P. de Saint Ours, and B. Talai (1989), Earthquakes of the Rabaul seismo-deformational crisis September 1983 to July 1985 seismicity on a ring fault, in *Volcanic Hazards: Assessment and Monitoring*, IAVCEI Proceedings in Volcanology, edited by J. H. Latter, pp. 429–462, Springer-Verlag, Berlin.
- Mori, J., R. A. White, D. H. Harlow, P. Okubo, J. A. Power, R. P. Hoblitt, E. P. Laguerta, A. Lanzuza, and B. C. Bautista (1996), Volcanic earthquakes following the 1991 climactic eruption of Mount Pinatubo: Strong seismicity during a waning eruption, in *Fire and Mud: Eruptions and Lahars of Mount Pinatubo, Philippines*, edited by C. G. Newhall and R. S. Punongbayan, pp. 339–350, Univ. of Washington Press, Seattle, Wash.
- Nakada, S., M. Nagai, T. Kaneko, A. Nozawa, and K. Suzuki-Kamata (2005), Chronology and products of the 2000 eruption of Miyakejima Volcano, Japan, *Bull. Volcanol.*, *67*, 205–218, doi:10.1007/s00445-004-0404-4.
- Nettles, M., and G. Ekström (1998), Faulting mechanism of anomalous earthquakes near Bárðarbunga Volcano, Iceland, *J. Geophys. Res.*, *103*(B8), 17,973–17,983.
- Ohminato, T., and H. Kumagai (2001), On the very-long-period seismic pulses observed during the 2000 Miyake-jima volcanic activity (in Japanese with English abstract), paper presented at Volcanic Structure in the Shallow Part and Volcanic Fluid, Disaster Prevention Research Institute, Kyoto University, available at <http://www.dpri.kyoto-u.ac.jp/~kazan/12k03/ohminato.pdf>.
- Pechmann, J. C., W. R. Walter, S. J. Nava, and W. J. Arabasz (1995), The February 3, 1995,  $M_L$  5.1 seismic event in the Trona Mining District of Southwestern Wyoming, *Seism. Res. Lett.*, *66*(3), 25–34.
- Pechmann, J. C., W. J. Arabasz, K. L. Pankow, and R. Burlacu (2008), Seismological report on the 6 August 2007 Crandall Canyon Mine Collapse in Utah, *Seism. Res. Lett.*, *79*(5), 620–636, doi:10.1785/gssrl.79.5.620.
- Prejean, S., A. Stork, W. Ellsworth, D. Hill, and B. Julian (2003), High precision earthquake locations reveal seismogenic structure beneath Mammoth Mountain, California, *Geophys. Res. Lett.*, *30*(24), doi:10.1029/2003GL018334.
- Reynolds, R. W., D. Geist, and M. D. Kurz (1995), Physical volcanology and structural development of Sierra Negra volcano, Isabela Island, Galápagos archipelago, *Geol. Soc. Am. Bull.*, *107*(12), 1398–1410, doi:10.1130/0016-7606(1995)107<1398:PVASDO>2.3.CO;2.
- Richards, P. G., and W.-Y. Kim (2005), Equivalent volume sources for explosions at depth: Theory and observations, *Bull. Seism. Soc. Am.*, *95*(2), 401–407, doi:10.1785/0120040034.
- Roche, O., T. H. Druitt, and O. Merle (2000), Experimental study of caldera formation, *J. Geophys. Res.*, *105*(B1), 395–416.
- Ross, A., G. R. Foulger, and B. R. Julian (1996), Non-double-couple earthquake mechanisms at the Geysers geothermal area, California, *Geophys. Res. Lett.*, *23*, 877–880.
- Rubin, A. M. (1995), Propagation of magma-filled cracks, *Annu. Rev. Earth Planet. Sci.*, *23*, 287–336.
- Rubin, A. M., and D. D. Pollard (1987), Origins of blade-like dikes in volcanic rift zones. In *Volcanism in Hawaii*, U.S. Geological Survey Prof. Paper 1350, edited by R. W. Decker and T. Wright, pp.1449–1470.
- Sammis, C. G., and B. R. Julian (1987), Fracture instabilities accompanying dike intrusion, *J. Geophys. Res.*, *92*(B3), 2597–2605.
- Saunders, S. J. (2001), The shallow plumbing system of Rabaul caldera: a partially intruded ring fault?, *Bull. Volcanol.*, *63*, 406–420, doi:10.1007/s004450100159.
- Saunders, S. J. (2005), The possible contribution of circumferential fault intrusion to caldera resurgence, *Bull. Volcanol.*, *67*, 57–71, doi:10.1007/s00445-004-0360-z.
- Scandone, R., and S. D. Malone (1985), Magma supply, magma discharge, and readjustment of the feeding system of Mount St. Helens during 1980, *J. Volcanol. Geophys. Res.*, *23*, 239–262.
- Self, S. (2012), The effects and consequences of very large explosive volcanic eruptions, *Phil. Trans. R. Soc. A*, *364*, 2073–2097, doi:10.1098/rsta.2006.1814.
- Self, S., L. Keszthelyi, and T. Thordarson (1998), The importance of pahoehoe, *Annu. Rev. Earth Planet. Sci.*, *26*, 81–110.
- Shuler, A., and G. Ekström (2009), Anomalous earthquakes associated with Nyiragongo Volcano: Observations and potential mechanisms, *J. Volcanol. Geotherm. Res.*, *181*(3–4), 219–230, doi:10.1016/j.jvolgeores.2009.01.011.

- Shuler, A., G. Ekström, and M. Nettles (2013), Global observation of vertical-CLVD earthquakes at active volcanoes, *J. Geophys. Res.*, *118*, 138–164, doi:10.1029/2012JB009721.
- Siebert, L., and T. Simkin (2002), *Volcanoes of the world: An Illustrated catalog of holocene volcanoes and their eruptions*, Smithsonian Institution, Global Volcanism Program, Digital Information Series, GVP-3, <http://www.volcano.si.edu/world>.
- Sobradelo, R., A. Geyer, and J. Marti (2010), Statistical data analysis of the CCDB (Collapse Caldera Database): Insights on the formation of caldera systems, *J. Volcanol. Geotherm. Res.*, *198*, 241–252.
- Taylor, S. R. (1994), False alarms and mine seismicity: An example from the Gentry Mountain Mining Region, Utah, *Bull. Seism. Soc. Am.*, *84*(2), 350–358.
- Templeton, D. C., and D. S. Dreger (2006), Non-double-couple earthquakes in the Long Valley Volcanic Region, *Bull. Seism. Soc. Am.*, *96*(1), 69–79, doi:10.1785/0120040206.
- Tkalčić, H., D. S. Dreger, G. R. Foulger, and B. R. Julian (2009), The puzzle of the 1996 Bárðarbunga, Iceland, earthquake: No volumetric component in the source mechanism, *Bull. Seism. Soc. Am.*, *99*(5), 3077–3085.
- Ukawa, M., E. Fujita, E. Yamamoto, Y. Okada, and M. Kikuchi (2000), The 2000 Miyakejima eruption: Crustal deformation and earthquakes observed by the NIED Miyakejima observation network, *Earth Planets Space*, *52*(8), xix–xxvi.
- Wald, D. J., and T. H. Heaton (1994), Spatial and temporal distribution of slip for the 1992 Landers, California Earthquake, *Bull. Seism. Soc. Am.*, *84*, 668–691.
- Wells, D. L., and K. J. Coppersmith (1994), New empirical relationships among magnitude, rupture length, rupture width, rupture area, and surface displacement, *Bull. Seism. Soc. Am.*, *84*(4), 974–1002.
- White, S. M., J. A. Crisp, and F. J. Spera (2006), Long-term volumetric eruption rates and magma budgets, *Geochem. Geophys. Geosys.*, *7*(3), doi:10.1029/2005GC001002.
- Wolfe, C. J., P. G. Okubo, G. Ekström, M. Nettles, and P. M. Shearer (2004), Characteristics of deep ( $\geq 13$  km) Hawaiian earthquakes and Hawaiian earthquakes west of 155.55°W, *Geochem. Geophys. Geosys.*, *5*(4), doi:10.1029/2003GC000618.
- Yamamoto, E., M. Ukawa, E. Fujita, Y. Okada, and M. Kikuchi (2001), Step-like tilt change occurred during the Caldera-forming stage of the 2000 Miyakejima Volcanic activity (in Japanese with English abstract), *J. Geogr.*, *110*(2), 181–190.
- Yun, S.-H. (2007), A mechanical model of the large-deformation 2005 Sierra Negra volcanic eruption derived from InSAR measurements, Ph.D. Thesis, Department of Geophysics, Stanford University, 125 pp.
- Zobin, V. M. (2011), *Introduction to Volcanic Seismology*, 2nd ed., p. 474, Elsevier, Amsterdam, The Netherlands.